Unraveling Microscopic Mechanisms in Condensed Matter Systems with Local Magnetic Field Probes

Prof. Martino Poggio
Dr. Jelena Trbovic

11 February 2021

Faraday’s iron filings

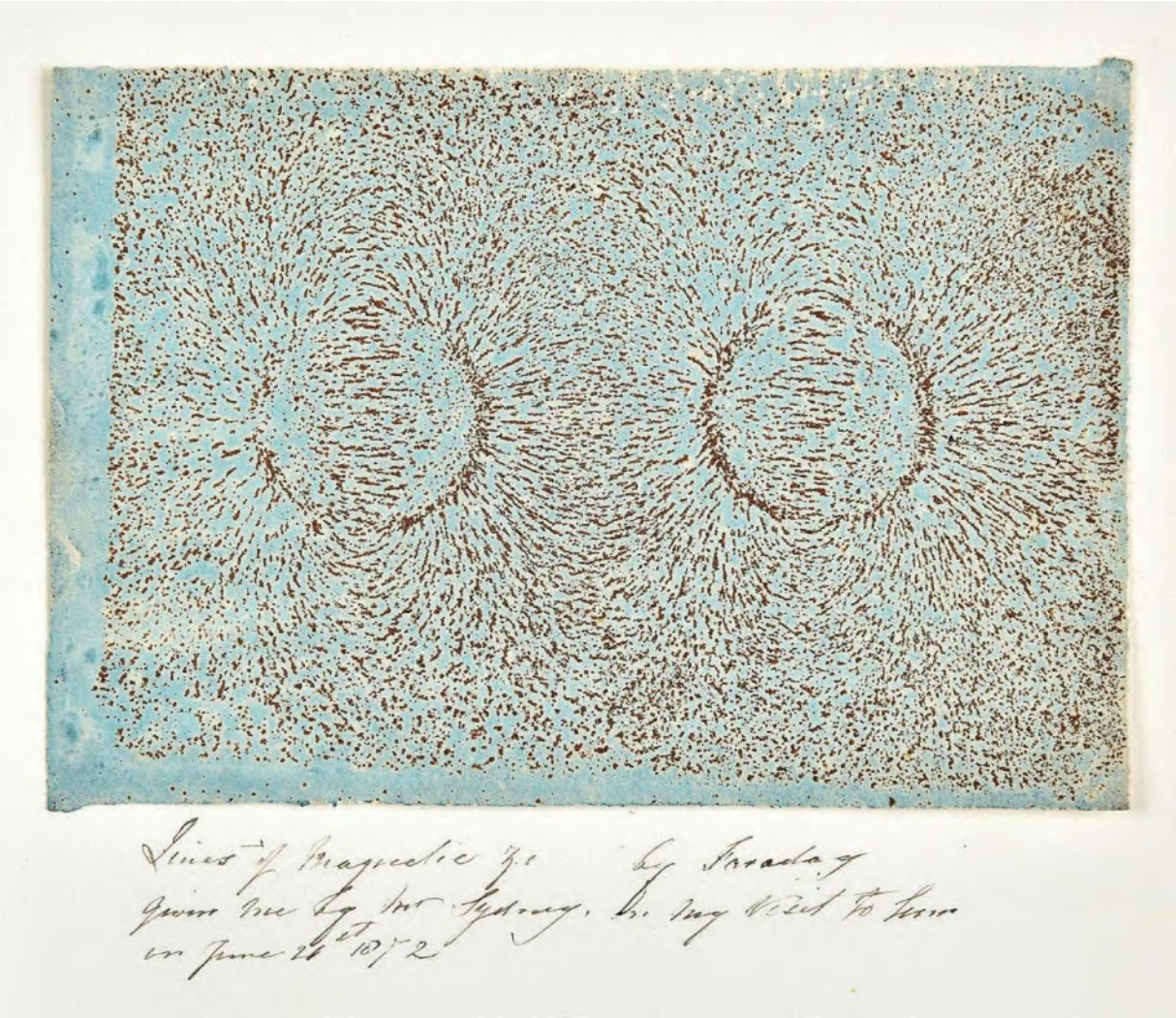

M. Faraday, ca. 1830s

Scanning tunnelling spectroscopy on atomic-scale

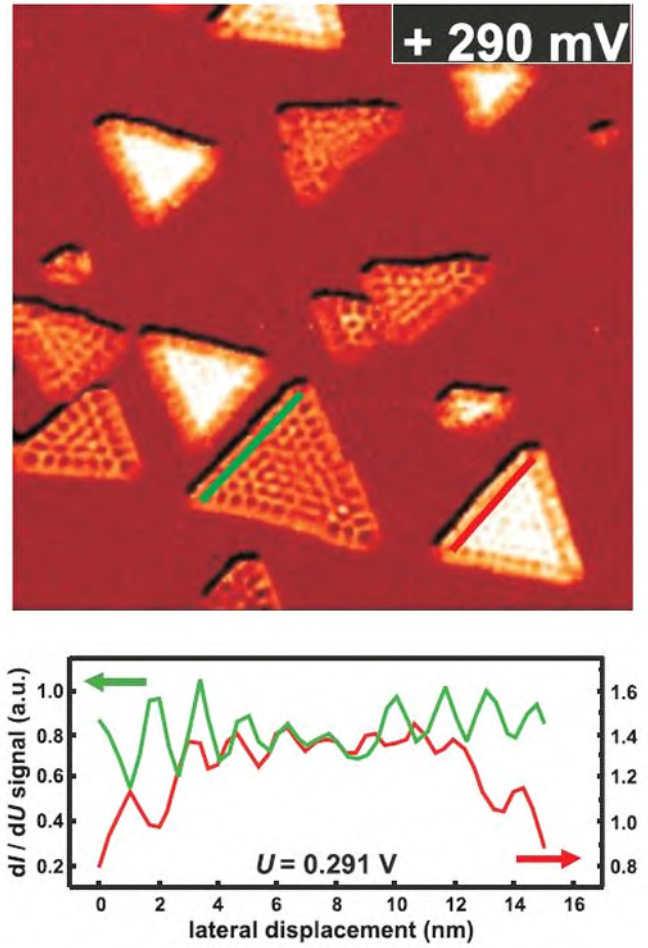

FIG. 44. (Color) SP-STS data (60×60 nm^2) revealing the spin dependence of the 2D electronic confinement states in nano-scale Co islands which manifests itself by a spin-dependent oscillation amplitude of the confinement states for differently magnetized Co nanoislands. From Pietzsch *et al.*, 2006.

Magneto-optical imaging of local spin-polarization

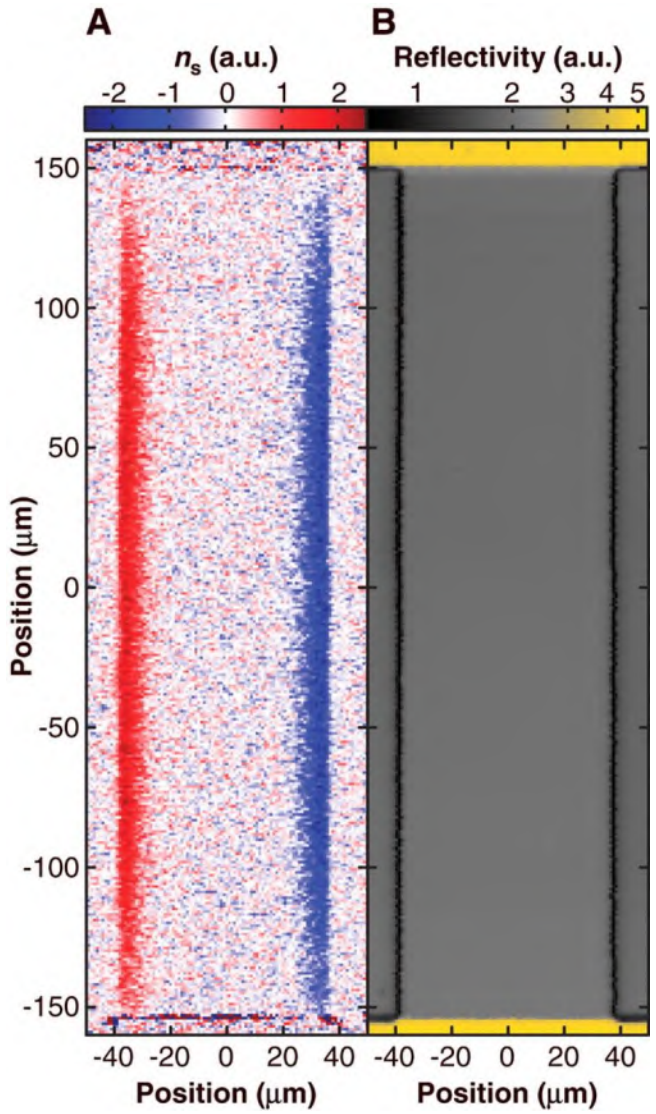

Kato et al., *Science* **306**, 5703 (2004).

Lorentz microscopy of skyrmion crystals

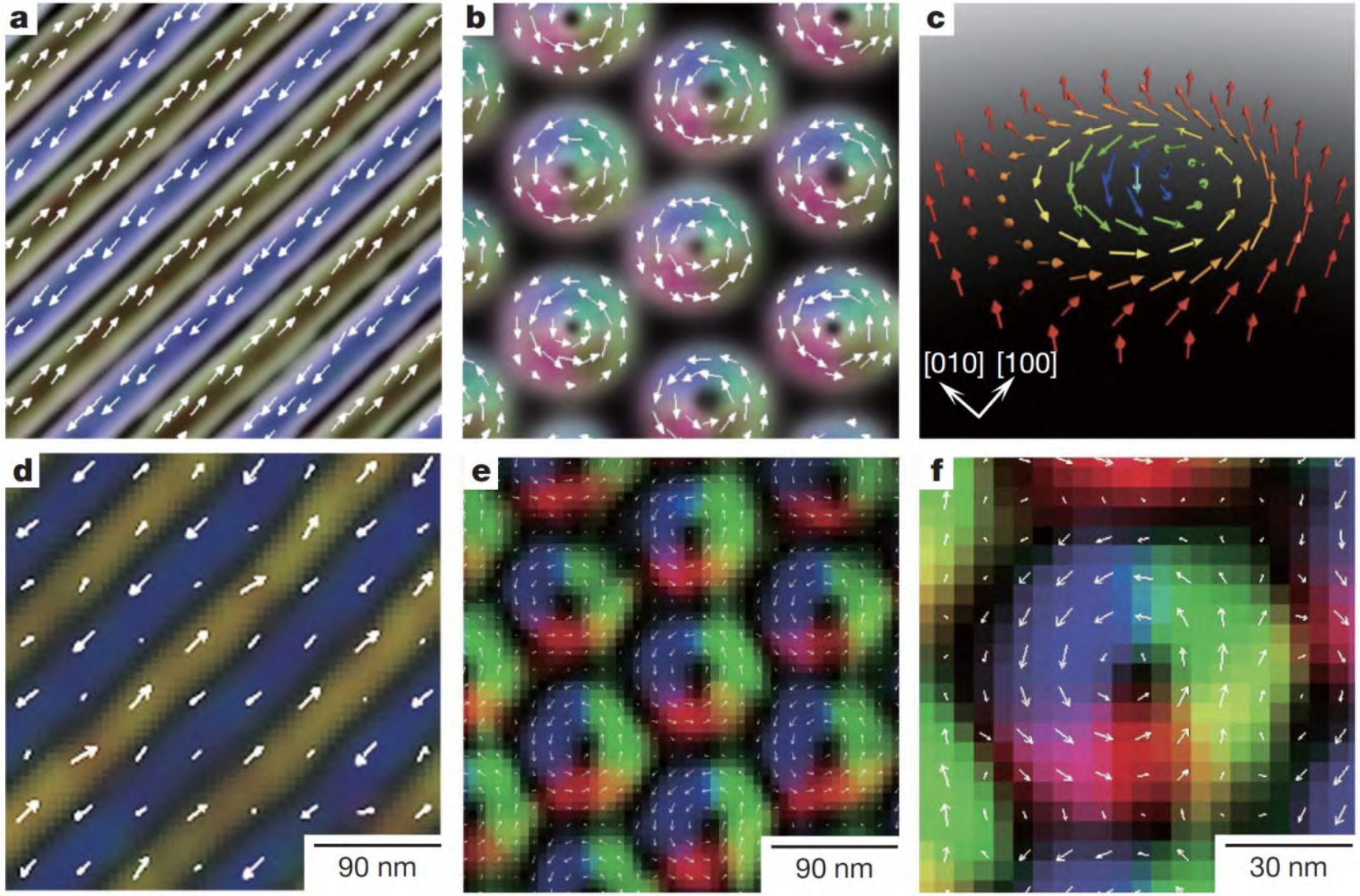

Yu et al., *Nature* **465**, 901 (2010).

SQUID microscopy of edge currents

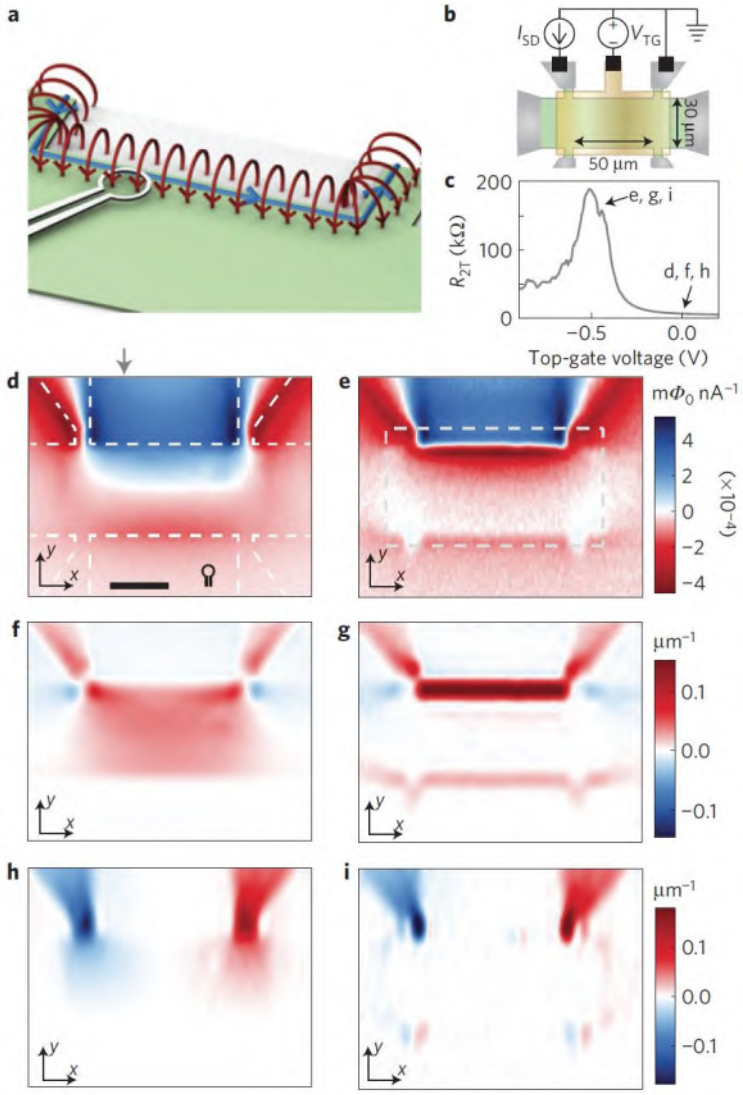

Nowack et al., *Nat. Phys.* **12**, 787 (2013).

Energence of 2D materials and vdW heterostructures

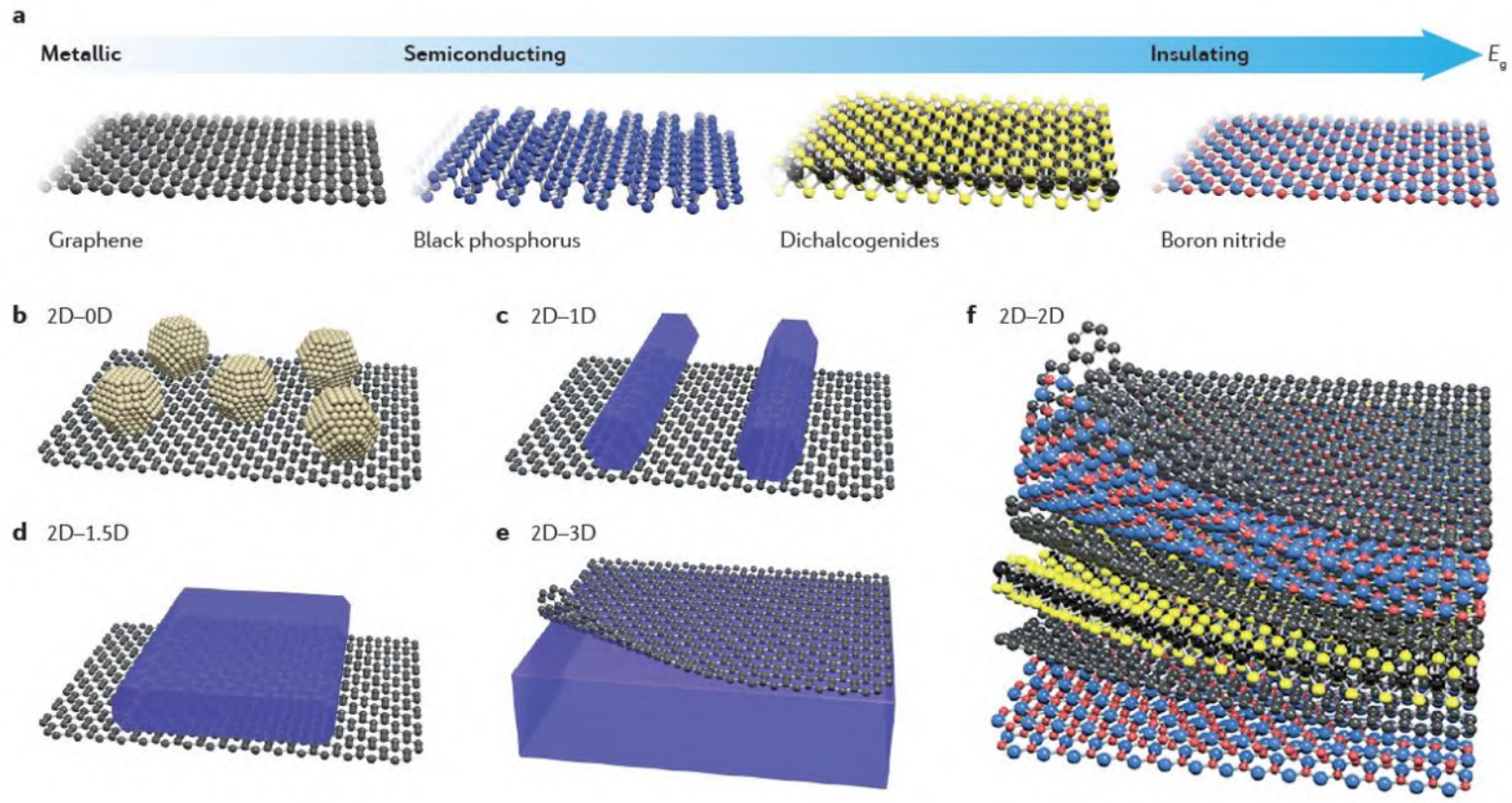

Figure 1 | **Two-dimensional layered materials and van der Waals heterostructures. a** | A broad library of two-dimensional layered materials (2DLMs) with varying chemical composition, atomic structures and electronic properties, with an increasing bandgap from left to right. **b**–**f** | Van der Waals heterostructures formed by integrating the dangling-bond-free 2DLMs with 0D nanoparticles or quantum dots (panel **b**), 1D nanowires (panel **c**), 1.5D nanoribbons (panel **d**), 3D bulk materials (panel **e**) and 2D nanosheets (panel **f**).

Liu et al., *Nat. Rev. Mater.* **1**, 1 (2016)

Energence of 2D materials and vdW heterostructures

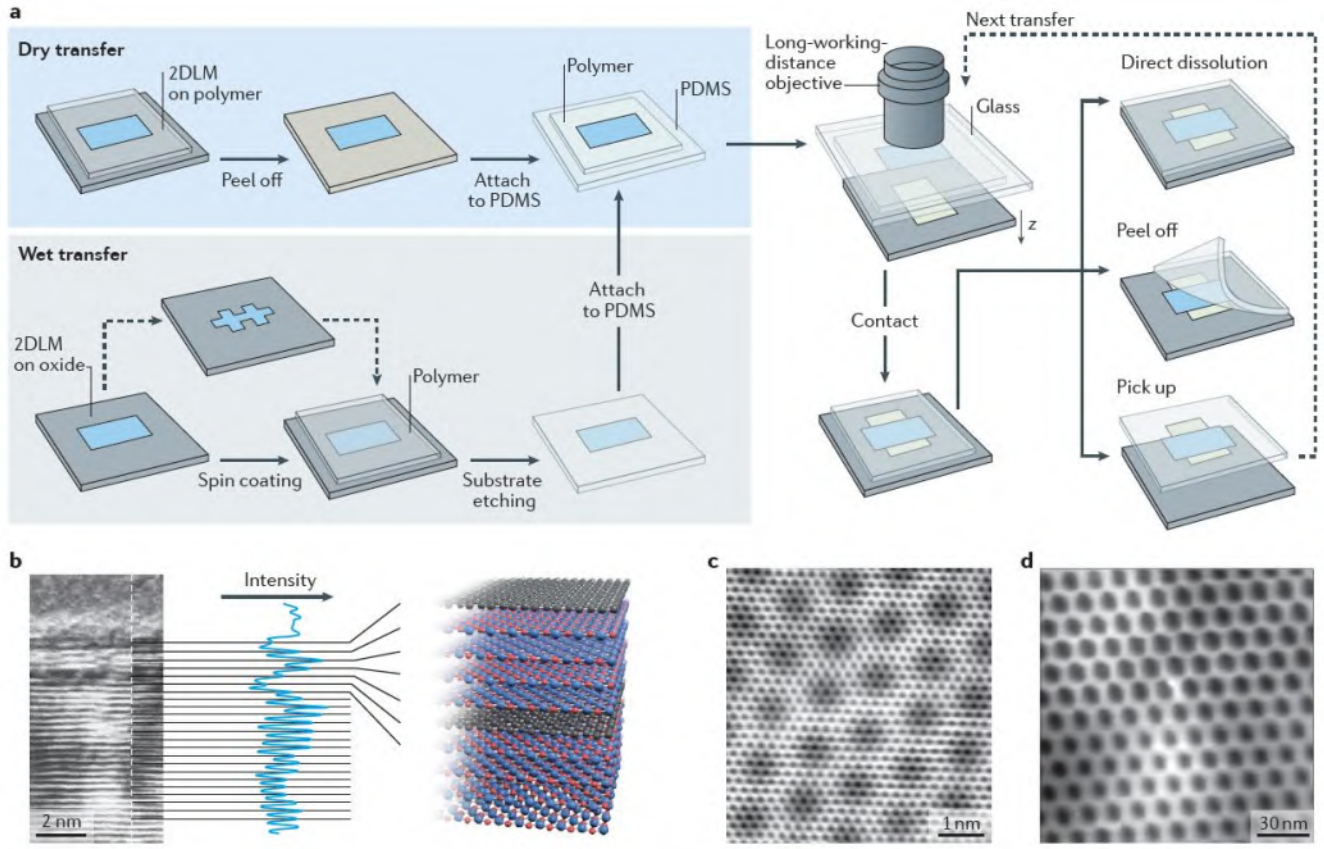

Figure 2 | **Assembly and characterization of 2D–2D vdWHs. a** | Schematic illustration of state-of-the-art alignment transfer processes for van der Waals heterostructure (vdWH) integration. Wet and dry transfer techniques are used to attach the target sheet to the stamp material. The stamp is then attached to a glass slide and placed in a transfer microscope. Micromanipulators allow for the precise alignment of sheets using a long-working-distance objective lens. The polymer transfer stamp can either be chemically dissolved away, mechanically peeled off or used to pick up the entire stack for further transfer steps. **b** | False-coloured high-resolution cross-sectional scanning tunnelling electron microscopy image of the BN–graphene–BN–graphene stack (left) and a corresponding schematic representation (right). **c**,**d** | Moiré pattern of graphene on BN (panel **c**) and a much larger moiré pattern of the commensurate–incommensurate transition of graphene on BN (panel **d**). 2DLM, two-dimensional layered material; BN, boron nitride; PDMS, poly(dimethyl siloxane). Panel **b** is from REF. 71, Nature Publishing Group. Panel **c** is courtesy of Brian LeRoy, University of Arizona, USA. Panel **d** is from REF. 73, Nature Publishing Group.

Liu et al., *Nat. Rev. Mater.* **1**, 1 (2016)

Correlated states in atomically layered materials

ARTICLE

doi:10.1038/nature26160

Unconventional superconductivity in magic-angle graphene superlattices

Yuan Cao[1], Valla Fatemi[1], Shiang Fang[2], Kenji Watanabe[3], Takashi Taniguchi[3], Efthimios Kaxiras[2,4] & Pablo Jarillo-Herrero[1]

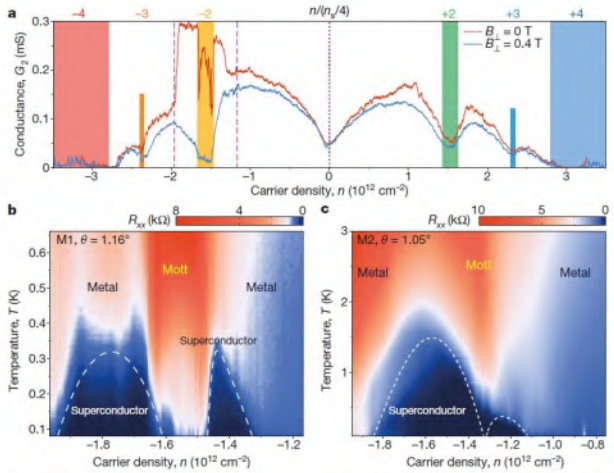

Figure 2 | Gate-tunable superconductivity in magic-angle TBG. **a**, Two-probe conductance $G_2 = I/V_{bias}$ of device M1 ($\theta = 1.16°$) measured in zero magnetic field (red) and at a perpendicular field of $B_\perp = 0.4$ T (blue). The curves exhibit the typical V-shaped conductance near charge neutrality ($n = 0$, vertical purple dotted line) and insulating states at the superlattice bandgaps $n = \pm n_s$, which correspond to filling ±4 electrons in each moiré unit cell (blue and red bars). They also exhibit reduced conductance at intermediate integer fillings of the superlattice owing to Coulomb interactions (other coloured bars). Near a filling of −2 electrons per unit cell, there is considerable conductance enhancement at zero field that is suppressed in $B_\perp = 0.4$ T. This enhancement signals the onset of superconductivity. Measurements were conducted at 70 mK; $V_{bias} = 10\,\mu$V. **b**, Four-probe resistance R_{xx}, measured at densities corresponding to the region bounded by pink dashed lines in **a**, versus temperature. Two superconducting domes are observed next to the half-filling state, which is labelled 'Mott' and centred around $-n_s/2 = -1.58 \times 10^{12}$ cm^{-2}. The remaining regions in the diagram are labelled as 'metal' owing to the metallic temperature dependence. The highest critical temperature observed in device M1 is $T_c = 0.5$ K (at 50% of the normal-state resistance). **c**, As in **b**, but for device M2, showing two asymmetric and overlapping domes. The highest critical temperature in this device is $T_c = 1.7$ K.

LETTER

doi:10.1038/nature22391

Layer-dependent ferromagnetism in a van der Waals crystal down to the monolayer limit

Bevin Huang[1]*, Genevieve Clark[2]*, Efrén Navarro-Moratalla[3]*, Dahlia R. Klein[3], Ran Cheng[4], Kyle L. Seyler[1], Ding Zhong[1], Emma Schmidgall[1], Michael A. McGuire[5], David H. Cobden[1], Wang Yao[6], Di Xiao[4], Pablo Jarillo-Herrero[3] & Xiaodong Xu[1,2]

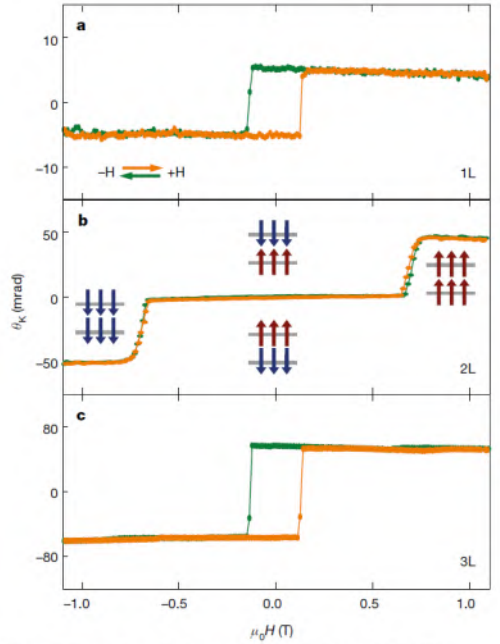

Figure 3 | Layer-dependent magnetic ordering in atomically-thin CrI_3. **a**, MOKE signal on a monolayer (1L) CrI_3 flake, showing hysteresis in the Kerr rotation as a function of applied magnetic field, indicative of ferromagnetic behaviour. **b**, MOKE signal from a bilayer CrI_3 showing vanishing Kerr rotation for applied fields ±0.65 T, suggesting antiferromagnetic behaviour. Insets depict bilayer (2L) magnetic ground states for different applied fields. **c**, MOKE signal on a trilayer (3L) flake, showing a return to ferromagnetic behaviour.

How to decipher the mechanism behind these phenomena?

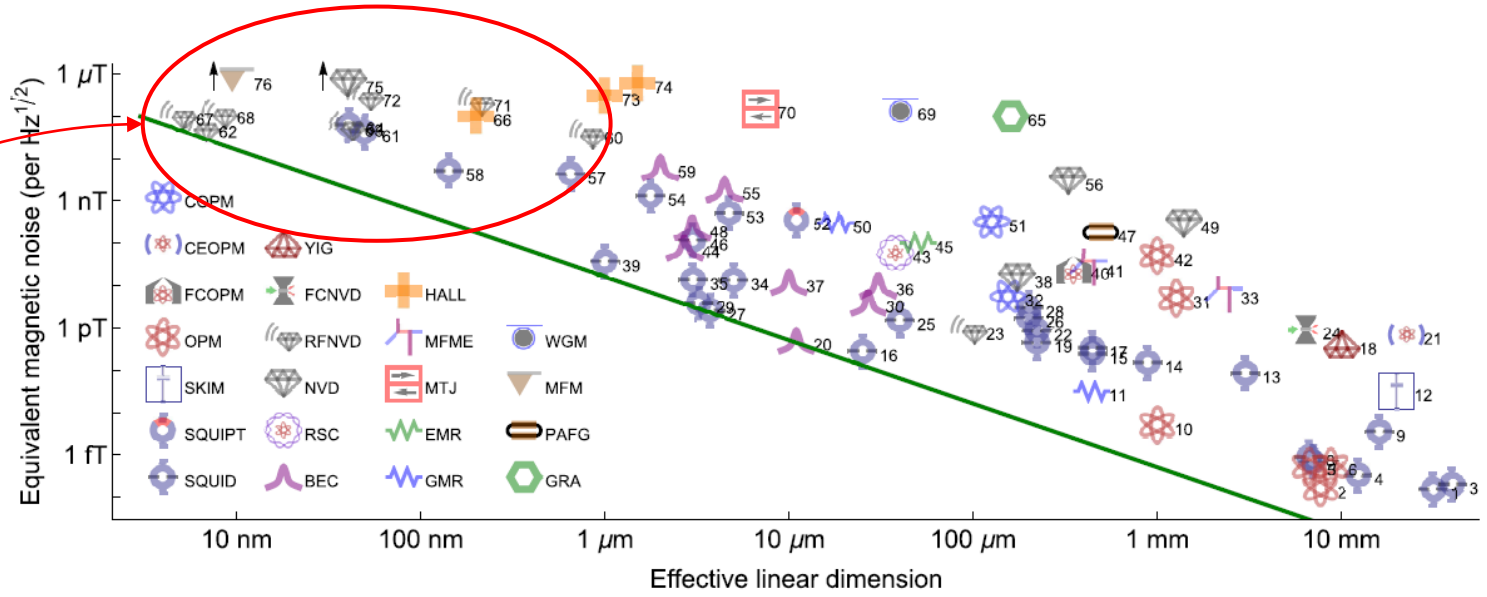

FIG. 2. Reported magnetic sensitivity $\delta B\sqrt{T}$ for different sensor technologies versus size of the sensitive region. Effective linear dimension l_{eff} indicates $\sqrt{\text{area}}$ for planar sensors and $\sqrt[3]{\text{volume}}$ for volumetric ones. For pointlike systems such as single spins, l_{eff} indicates $\sqrt[3]{\text{volume}}$ for a sphere with radius equal to the minimum source-detector distance. For work reporting sensitivity in units of magnetic dipole moment, we convert to field units using the reported sample distance. Excepting RFNVD, noise levels are the lowest reported value at frequency ≤ 1 kHz. An arrow indicates that the value is off the scale. SQUID, superconducting quantum interference device; SQUIPT, superconducting quantum interference proximity transistor; SKIM, superconducting kinetic impedance magnetometer; OPM, optically pumped magnetometer; FCOPM, OPM with flux concentrators; CEOPM, cavity-enhanced OPM; COPM, OPM with cold thermal atoms; BEC, Bose-Einstein condensate; RSC, Rydberg Schrödinger cat; NVD, nitrogen-vacancy center in diamond; RFNVD, radio-frequency NVD; FCNVD, NVD with flux concentrators; YIG, yttrium-aluminum-garnet; GMR, giant magnetoresistance; EMR, extraordinary magnetoresistance; MTJ, magnetic tunnel junction; MEMF, magnetoelectric multiferroic; HALL, Hall-effect sensor; GRA, graphene; PAFG, parallel gating fluxgate; MFM, magnetic force microscope, WGM, whispering-gallery mode magnetostrictive. Line shows $E_R \equiv \langle \delta B^2 \rangle T l_{\mathrm{eff}}^3/(2\mu_0) = \hbar$. Numeric labels refer to Table I.

Map weak magnetic field patterns with high spatial resolution

Mitchell & Palacios Alvarez, *Rev. Mod. Phys.* **92**, 021001 (2020)

Outline

- Scanning SQUID microscopy
  - SQUID-on-tip sensors
  - Magnetic imaging with SQUID-on-tip
- Zurich Instruments lock-in amplifiers
  - Measurement principles
  - Multiple mode measurement and control
- Magnetic force microscopy
  - Scaling down the sensor
  - NW MFM
- Comparison between techniques
  - Which sensor for which application?
  - Prospects for improvement

Superconducting quantum interference device (SQUID)

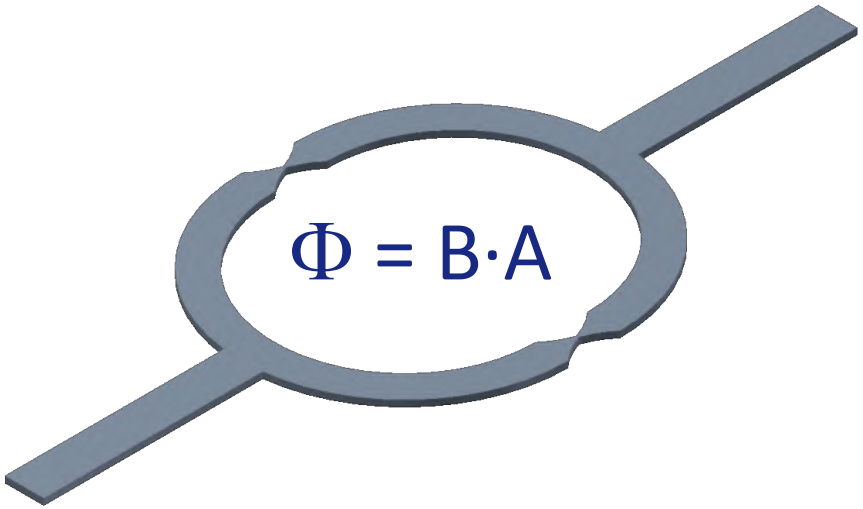

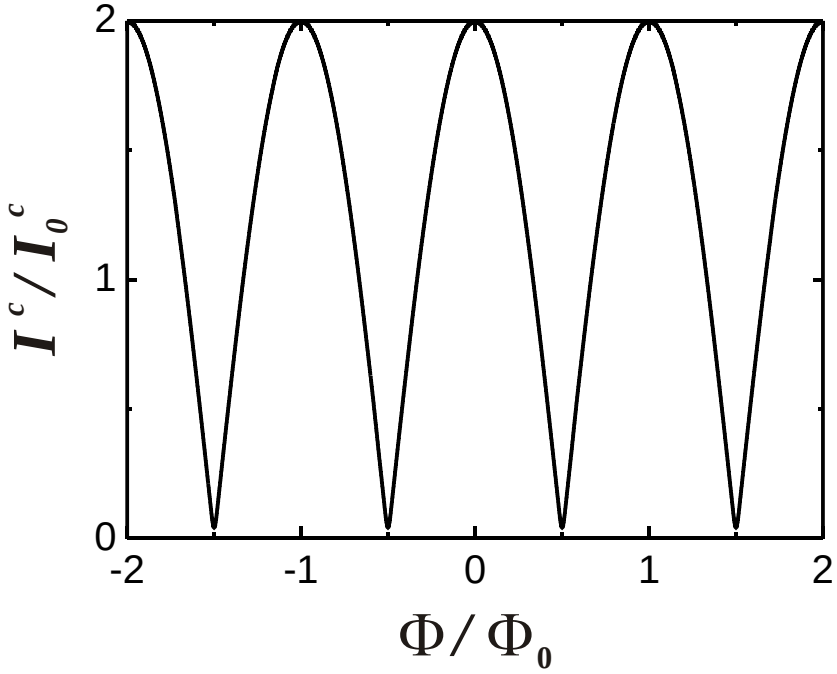

SQUID critical current: $I^c(\Phi) = 2I_0^C \cos|\pi\Phi/\Phi_0|$

SCANNING SQUID MICROSCOPY

John R. Kirtley
IBM T. J. Watson Research Center, Yorktown Heights, New York 10598;
e-mail: kirtley@watson.ibm.com

John P. Wikswo, Jr.
Department of Physics and Astronomy, Vanderbilt University, Nashville,
Tennessee 37235; e-mail: wikswojp@ctrvax.vanderbilt.edu

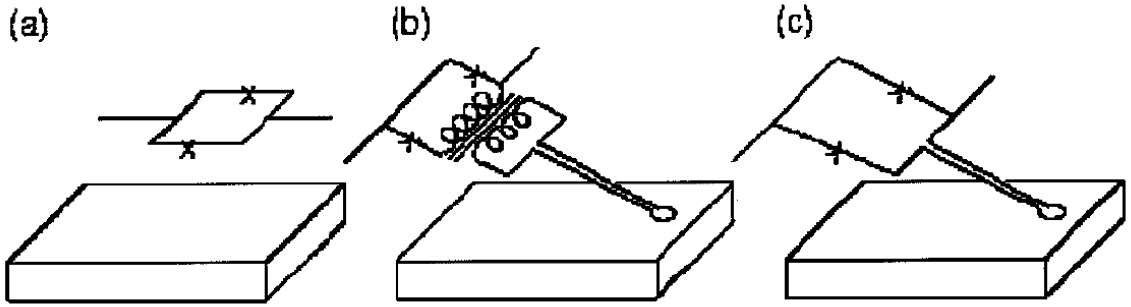

Annu. Rev. Mater. Sci. 1999. 29:117–48

Self-Aligned Nanoscale SQUID on a Tip

Amit Finkler,*,† Yehonathan Segev,† Yuri Myasoedov,† Michael L. Rappaport,† Lior Ne'eman,† Denis Vasyukov,† Eli Zeldov,† Martin E. Huber,‡ Jens Martin,§ and Amir Yacoby§

†Department of Condensed Matter Physics, Weizmann Institute of Science, Rehovot 76100, Israel, ‡Departments of Physics and Electrical Engineering, University of Colorado, Denver, Colorado 80217, and §Department of Physics, Harvard University, Cambridge, Massachusetts 02138

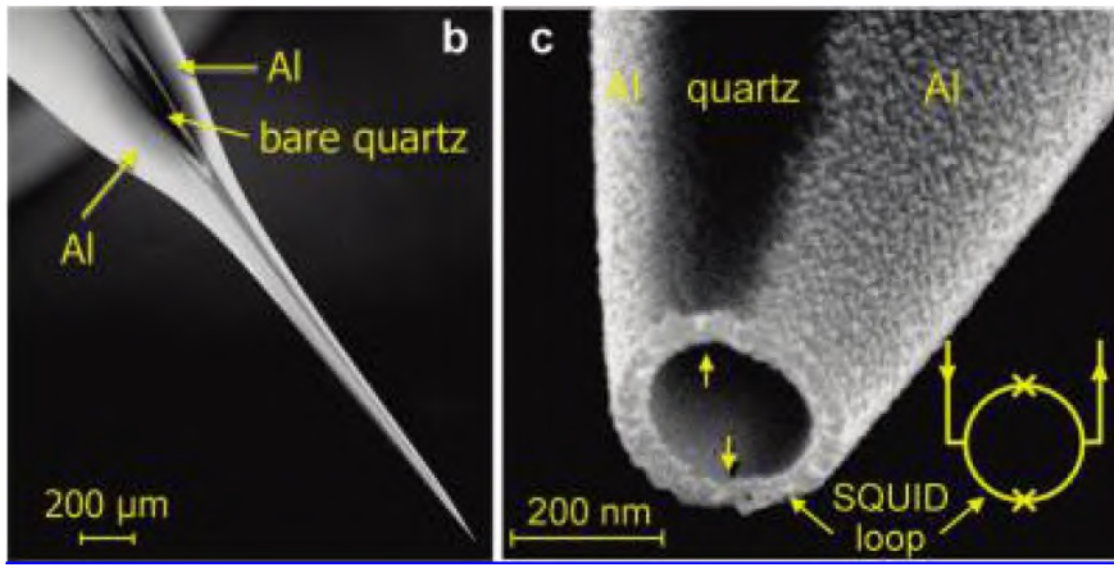

Nano Lett. **2010,** *10,* 1046–1049

SQUID-on-tip sensor

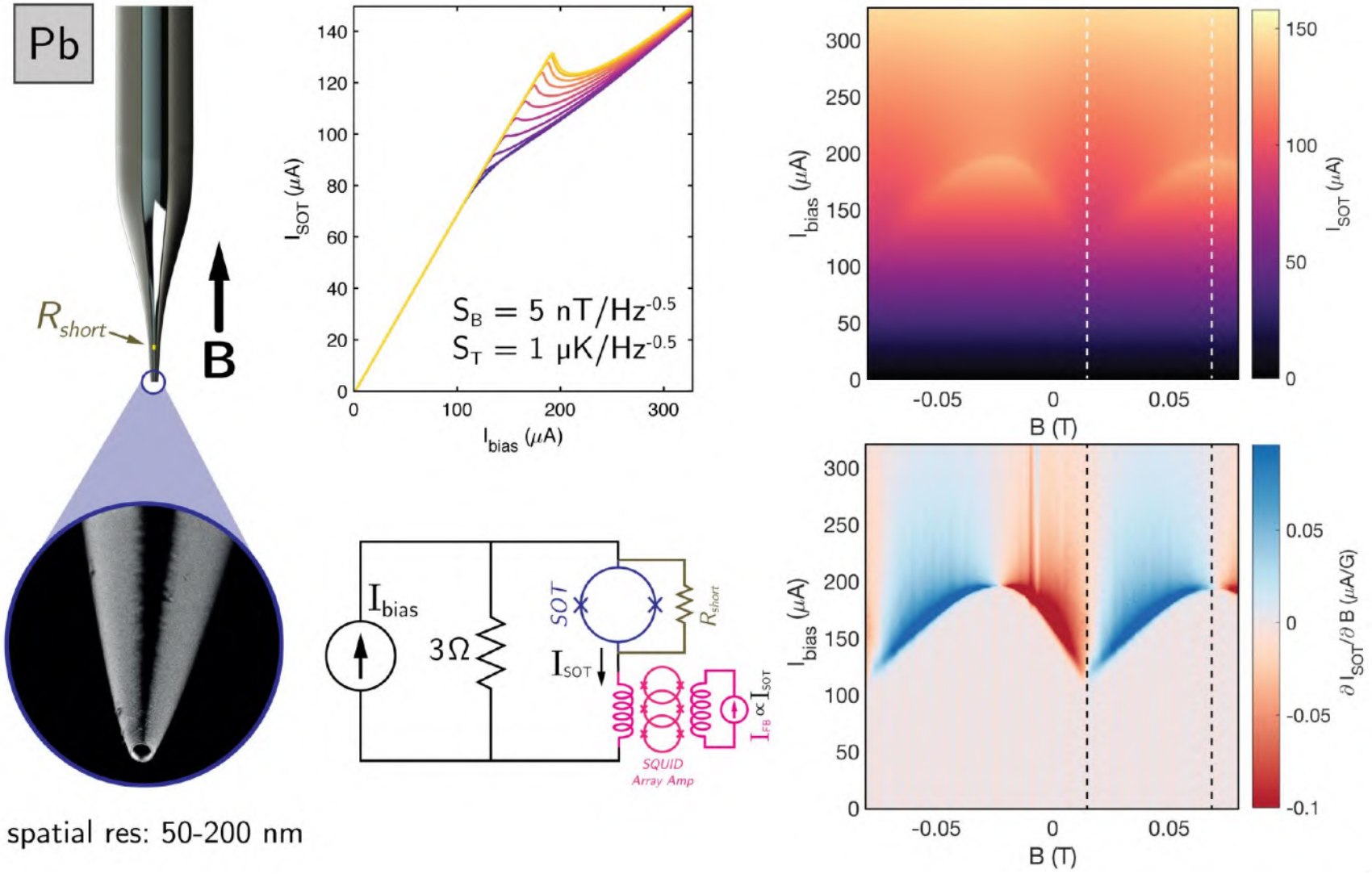

Vasyukov et al., *Nat. Nanotechnol.* **8**, 639 (2013)

Artificial spin ice

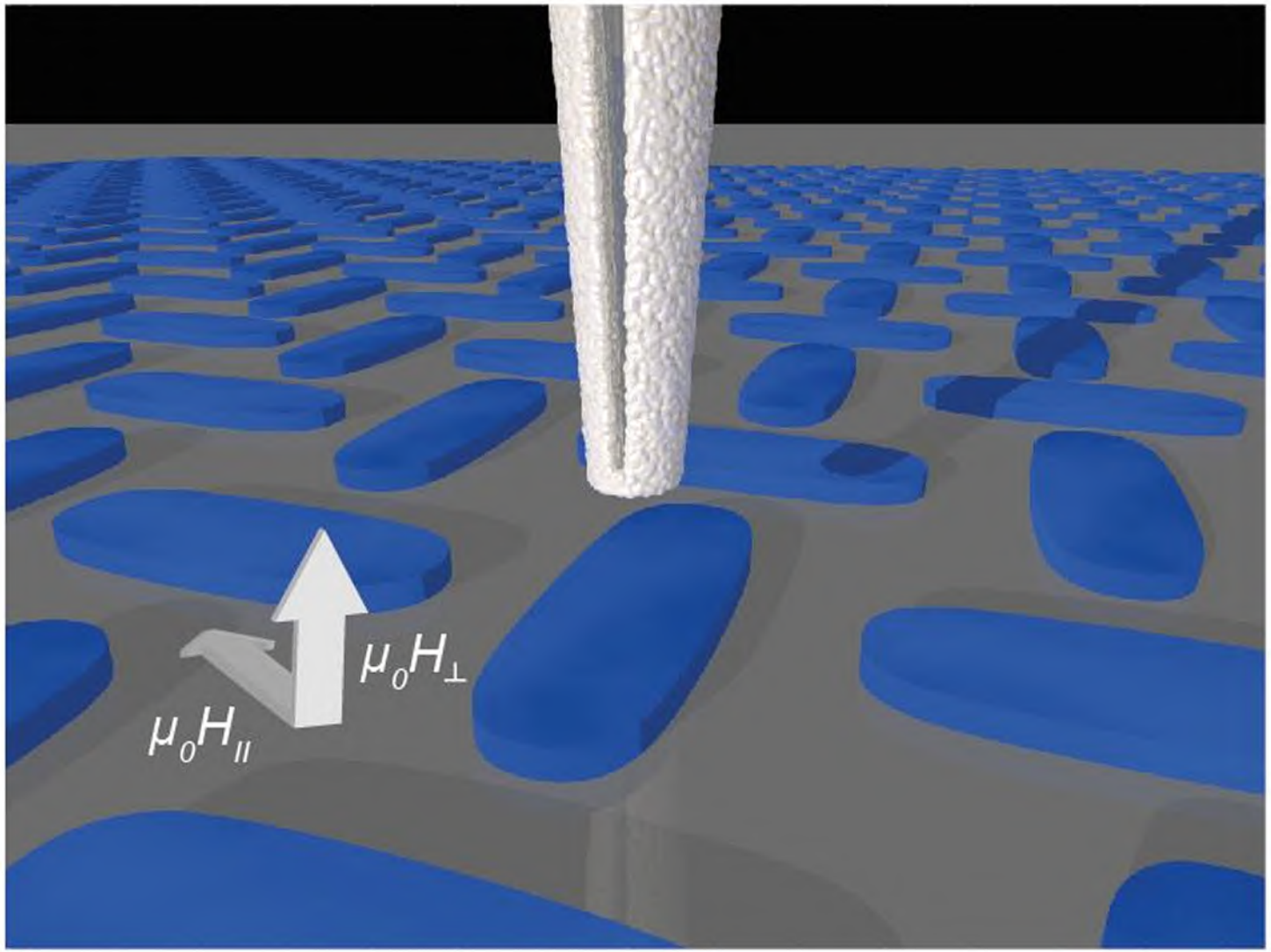

Wyss et al., *ACS Nano* **13**, 13910 (2019).

In reality…

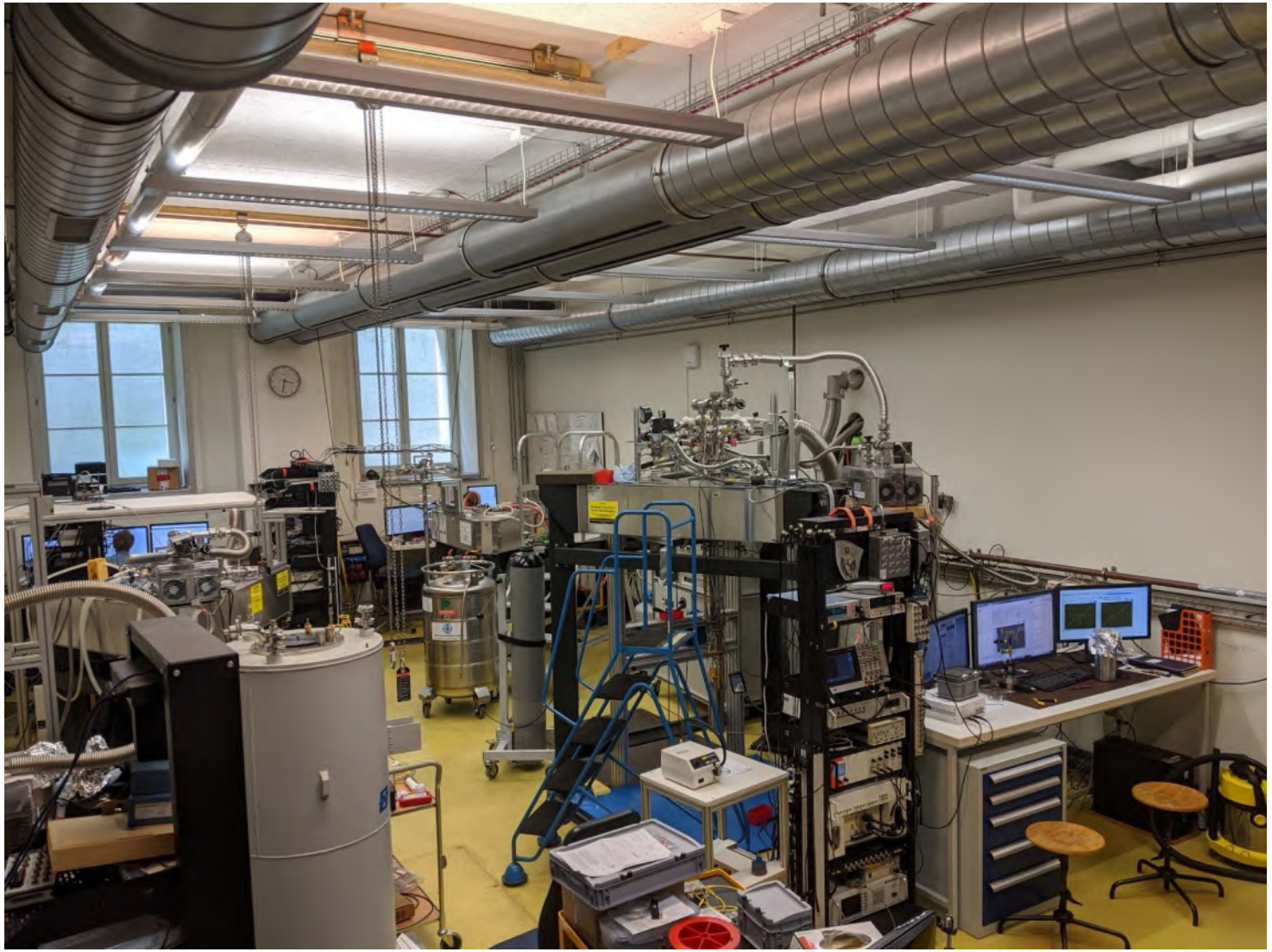

In reality…

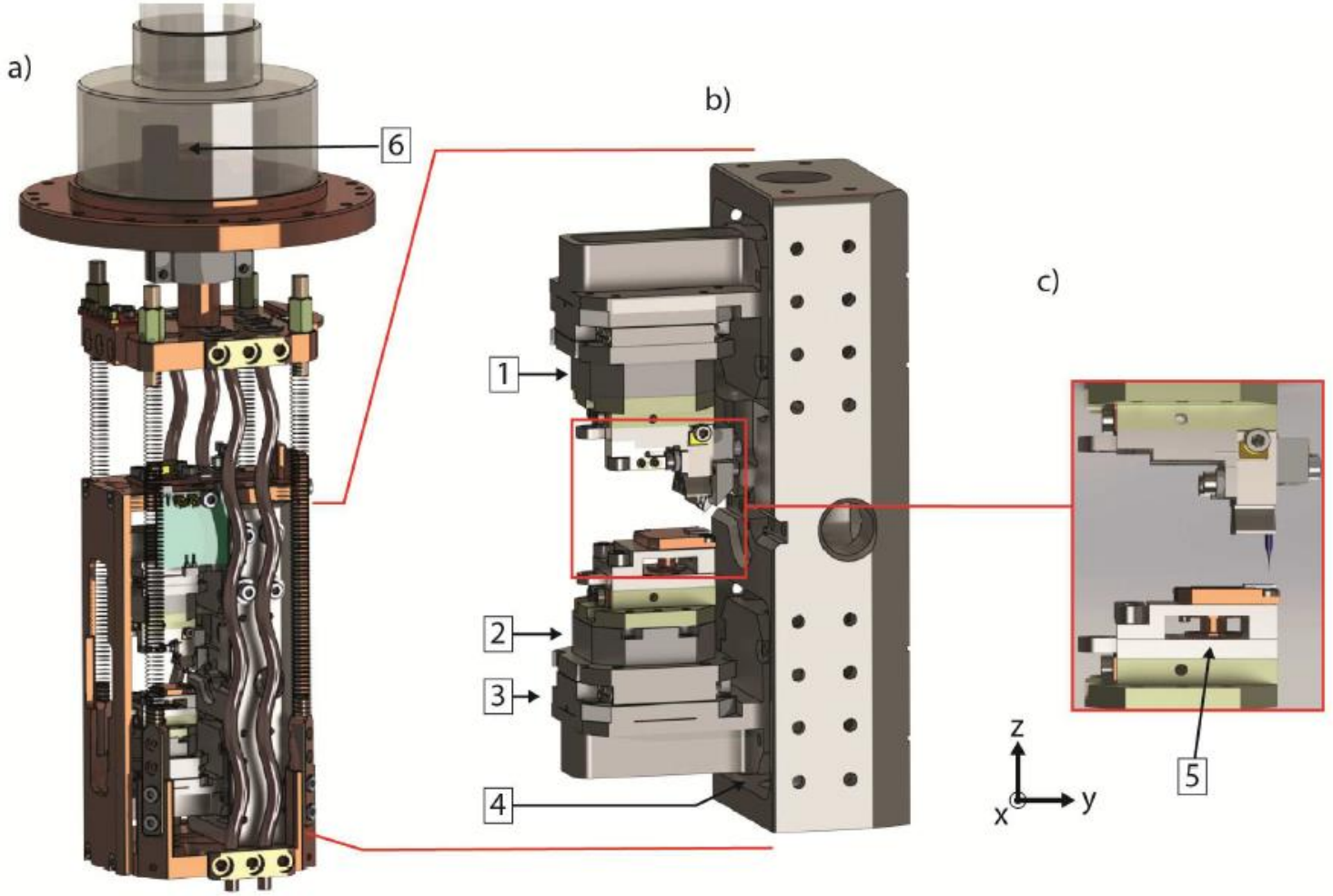

Ceccarelli, *Ph.D. Thesis in Physics,* University of Basel (2020).

Artificial spin ice

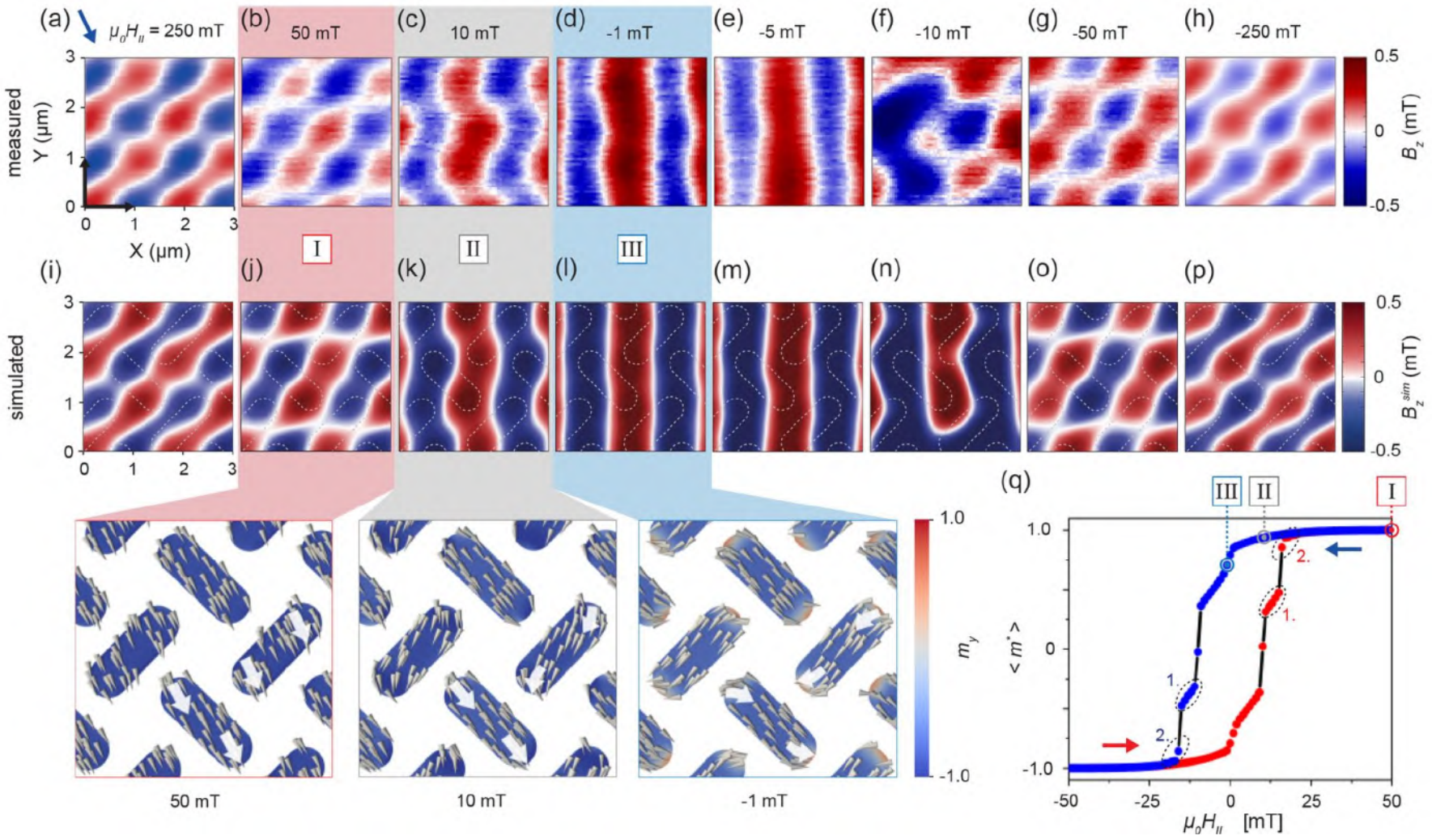

Wyss et al., *ACS Nano* **13**, 13910 (2019).

Superconducting vortices in a MoSi thin film

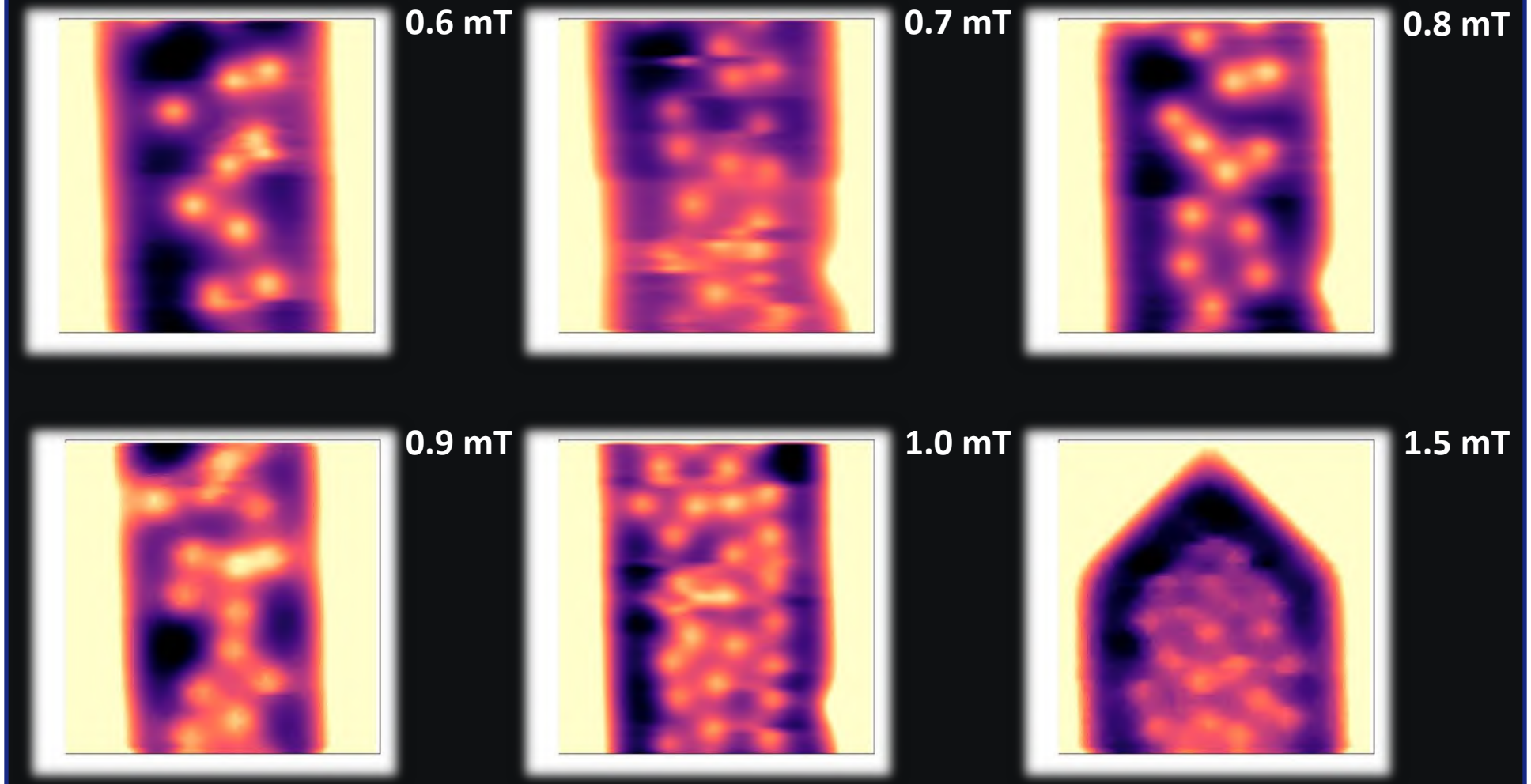

40 s per frame

Ceccarelli et al., *Phys. Rev. B* **100**, 104504 (2019).

Dynamics and flow of superconducting vortices

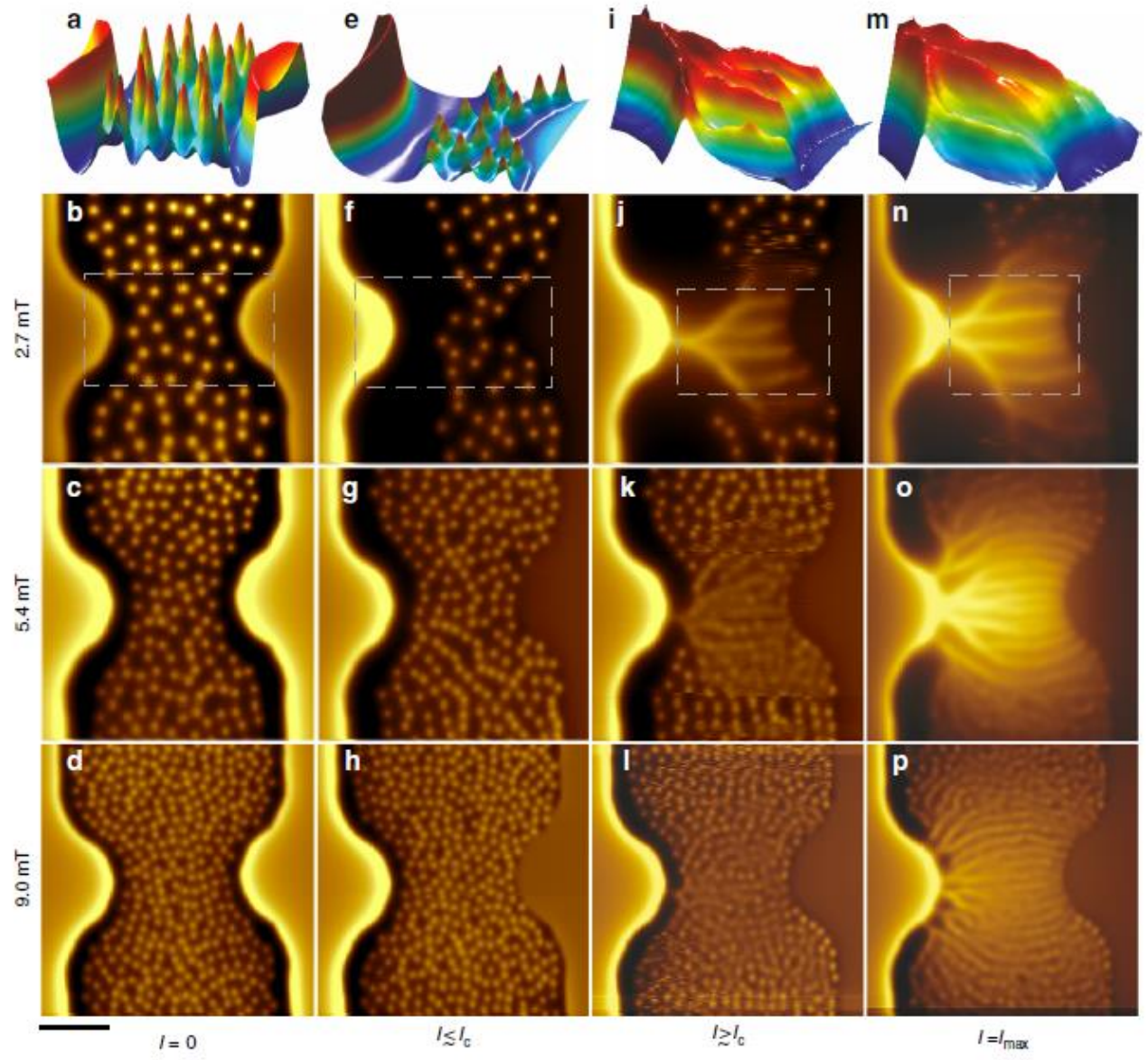

Embon et al., *Nat. Commun.* **8**, 85 (2017).

Outlook: superconducting qubit devices

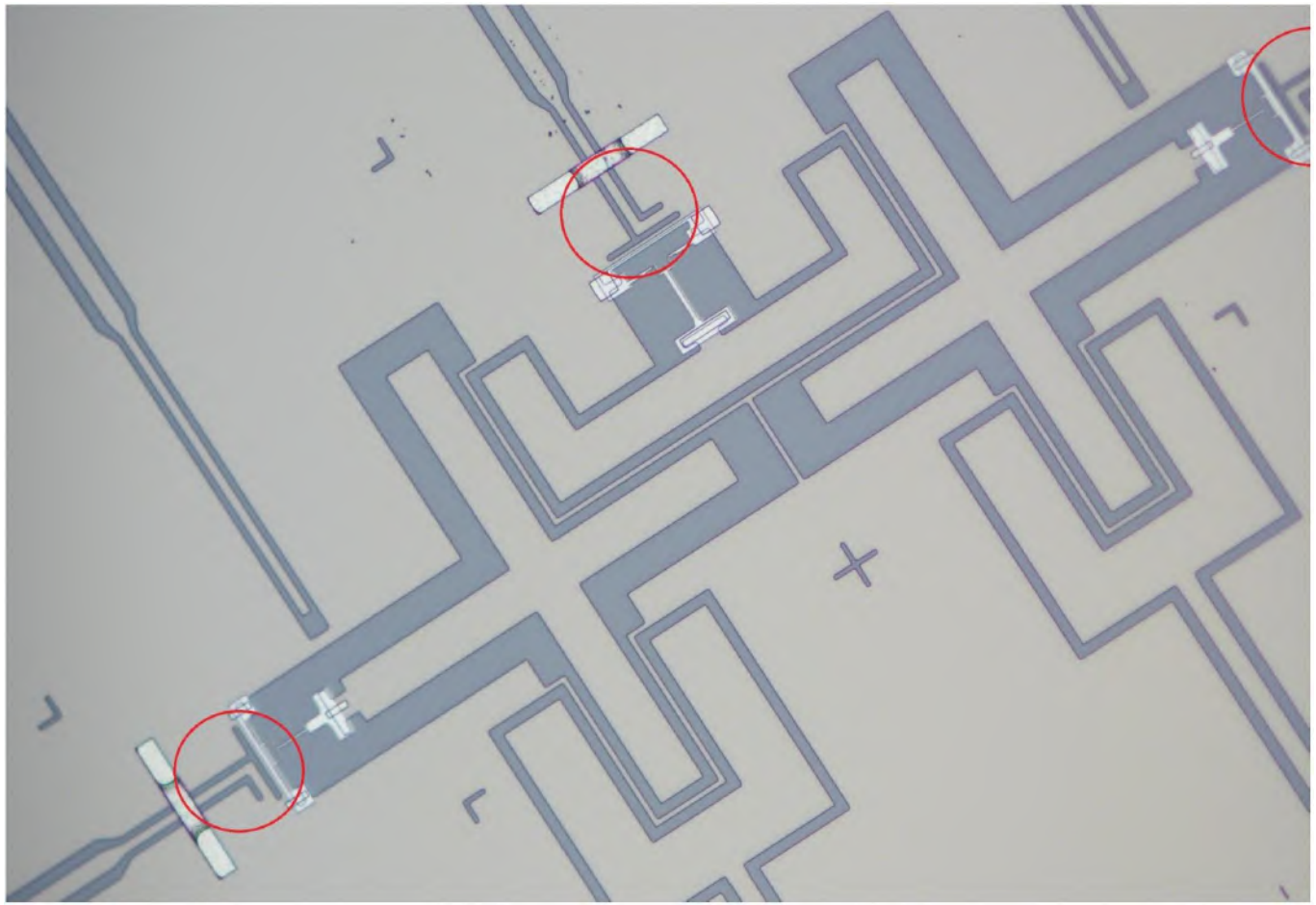

Nb qubit from Wallraff group (ETHZ).

Outlook: superconducting qubit devices

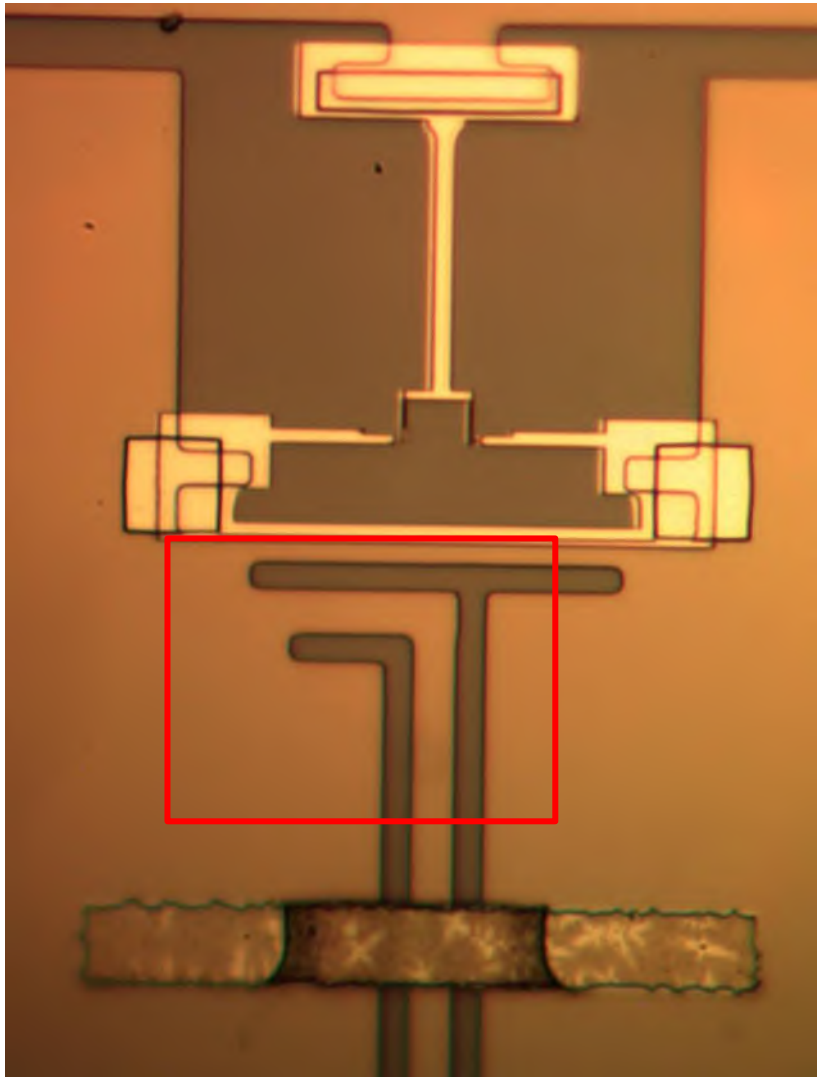

Nb qubit from Wallraff group (ETHZ).

Current flow in superconducting qubits

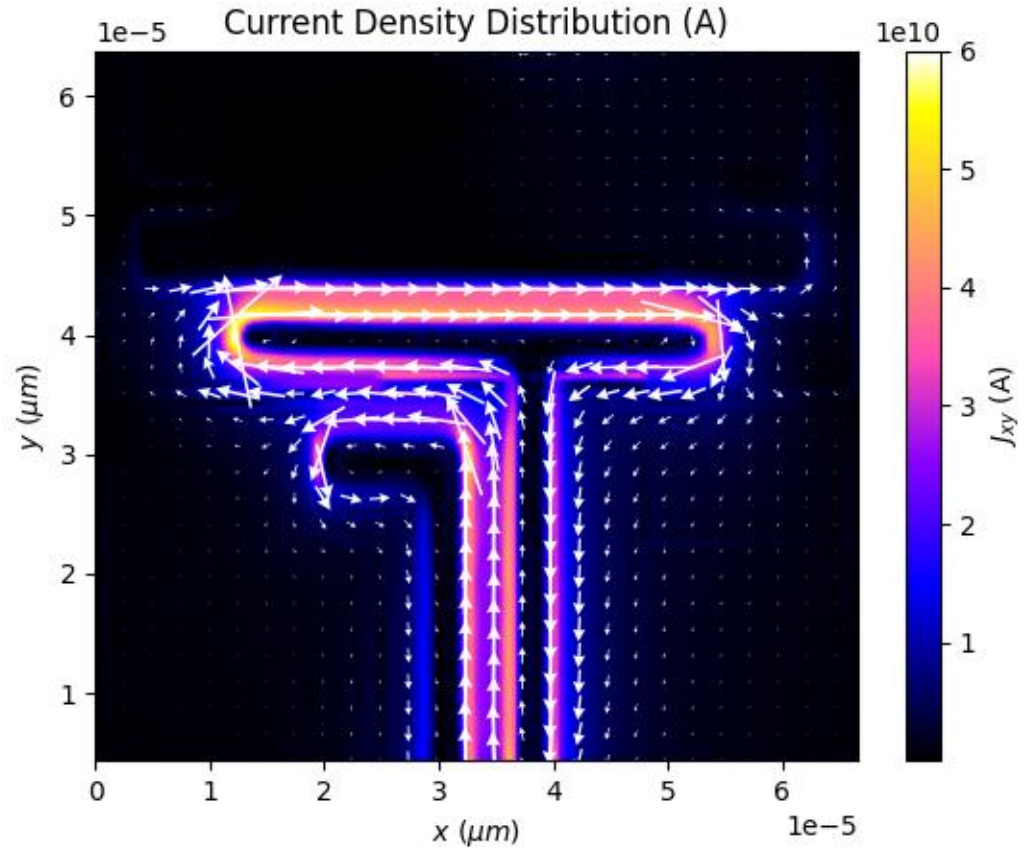

Nb qubit from Wallraff group; images from Poggio group

SQUID microscopy of quantum Hall edge currents

LETTERS
https://doi.org/10.1038/s41567-019-0713-3
nature physics

Nanoscale imaging of equilibrium quantum Hall edge currents and of the magnetic monopole response in graphene

Aviram Uri[1*], Youngwook Kim[2,3], Kousik Bagani[1], Cyprian K. Lewandowski[4], Sameer Grover[1], Nadav Auerbach[1], Ella O. Lachman[1,6], Yuri Myasoedov[1], Takashi Taniguchi[5], Kenji Watanabe[5], Jurgen Smet[2] and Eli Zeldov[1*]

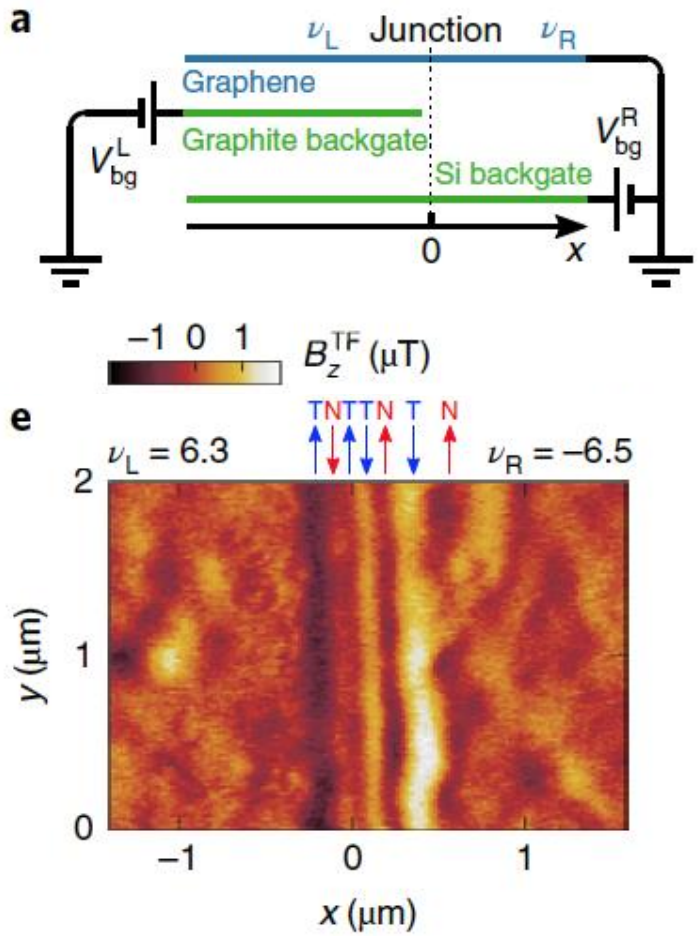

Uri et al., *Nat. Phys.* **16**, 164 (2020).

SQUID microscopy of twist-angle disorder

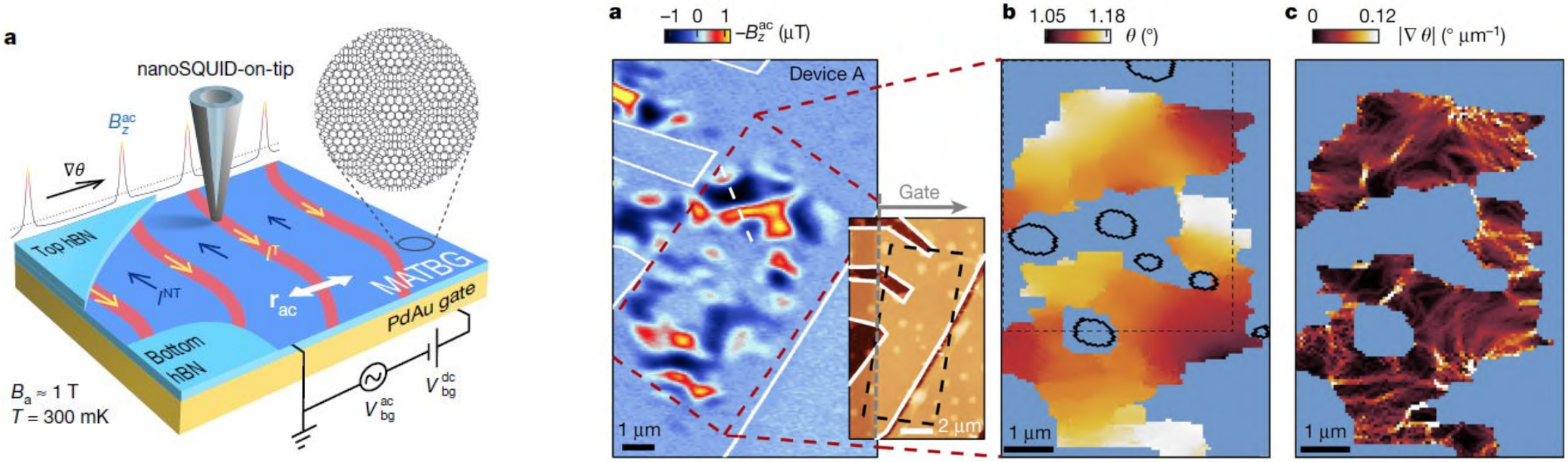

Uri et al., *Nature* **581**, 47 (2020).

Outline

- Scanning SQUID microscopy
  - SQUID-on-tip sensors
  - Magnetic imaging with SQUID-on-tip

- Zurich Instruments lock-in amplifiers
  - Measurement principles
  - Multiple mode measurement and control

- Magnetic force microscopy
  - Scaling down the sensor
  - NW MFM

- Comparison between techniques
  - Which sensor for which application?
  - Prospects for improvement

Zurich Instruments

Zurich Instruments Lock-in Amplifiers Enabling Discovery

Jelena Trbovic, Application Scientist

Zurich Instruments

What do we do?

experience LabOne

Hardware

- Adequate speed
- High sensitivity
- Low noise
- High resolution

+

Software

- Efficient workflows
- Functionality & features
- UI & APIs
- Value added over time

→

Instruments

- Quantum control systems
- Lock-in amplifiers
- Boxcar averagers
- Impedance analyzers

Zurich Instruments lock-in amplifiers

Enabling discovery

MFLI
500 kHz/ 5 MHz

HF2LI
50 MHz

UHFLI
600 MHz

experience LabOne

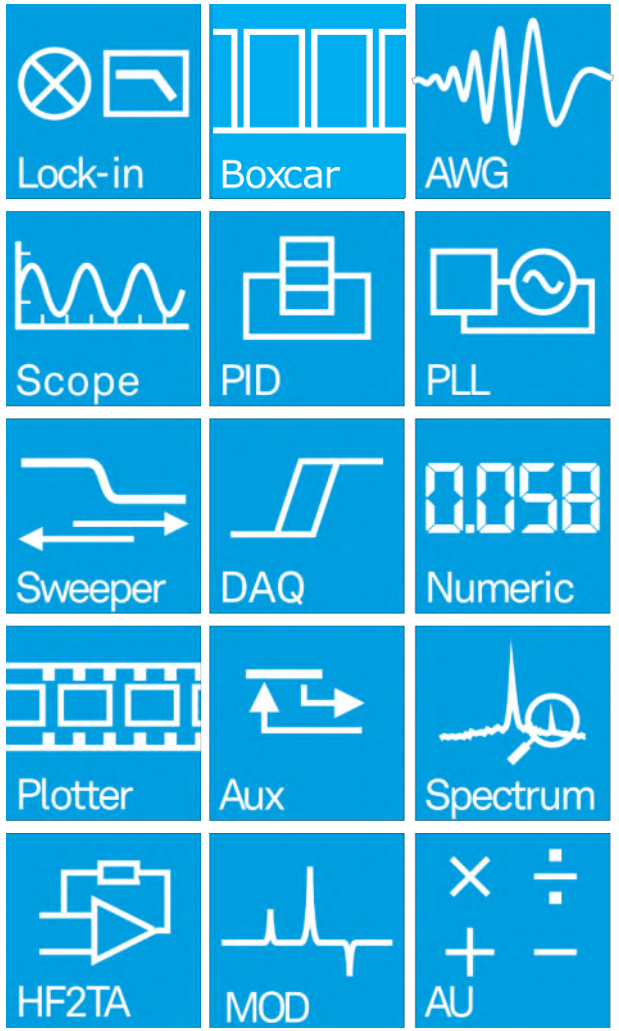

Why use lock-in amplifiers?

Small signals surrounded by noise are difficult to detect

Time domain

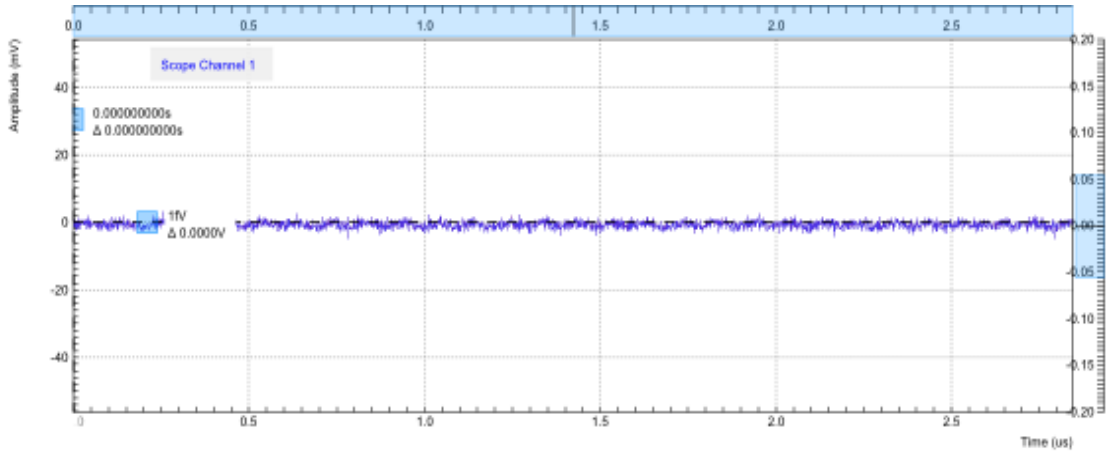

SNR ~ 10

Frequency domain

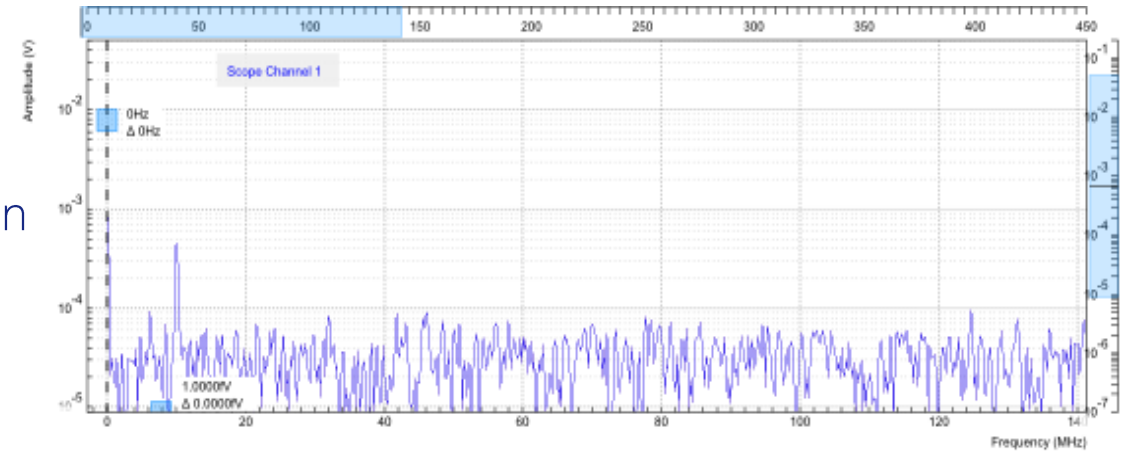

Why use lock-in amplifiers?

Noise spectrum

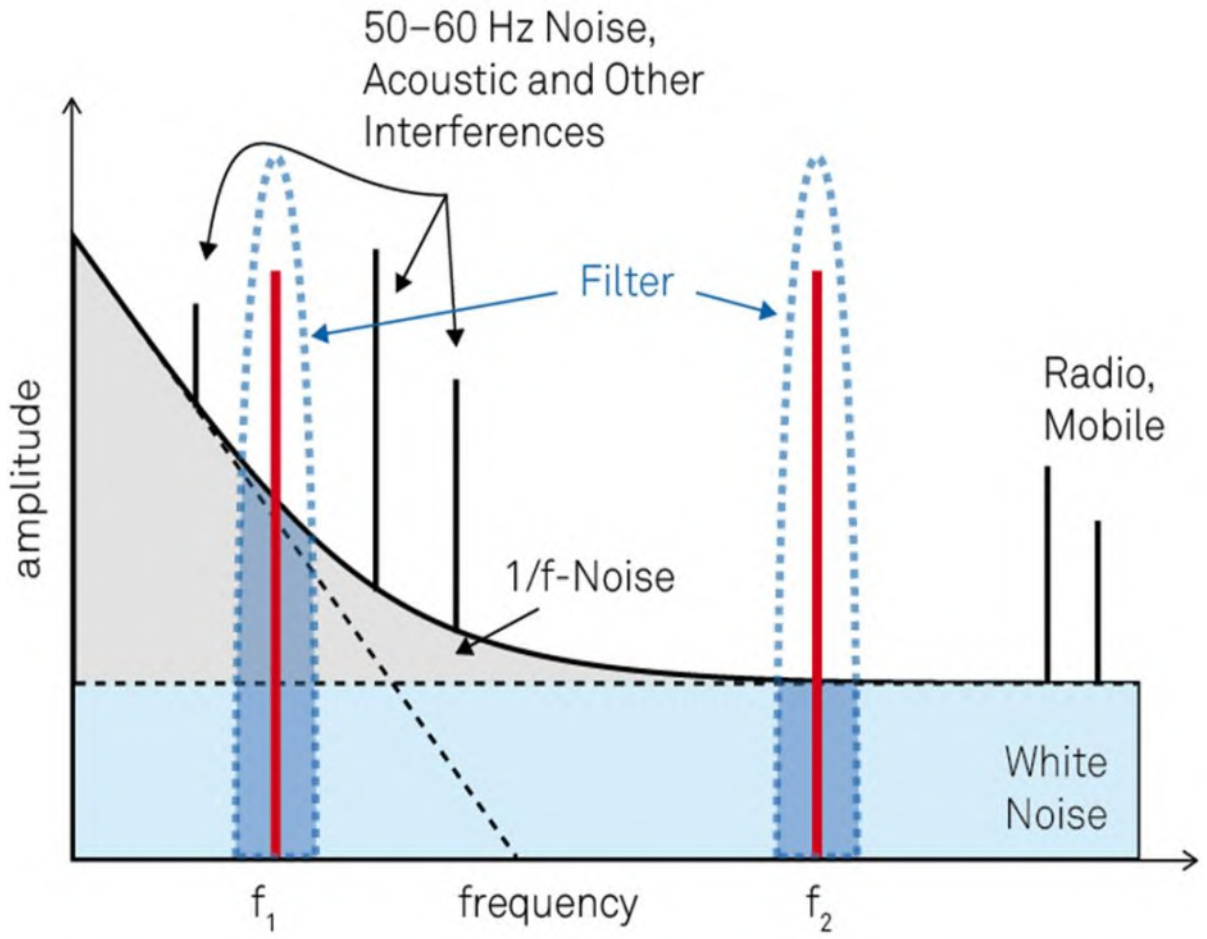

What does lock-in amplifier measure?

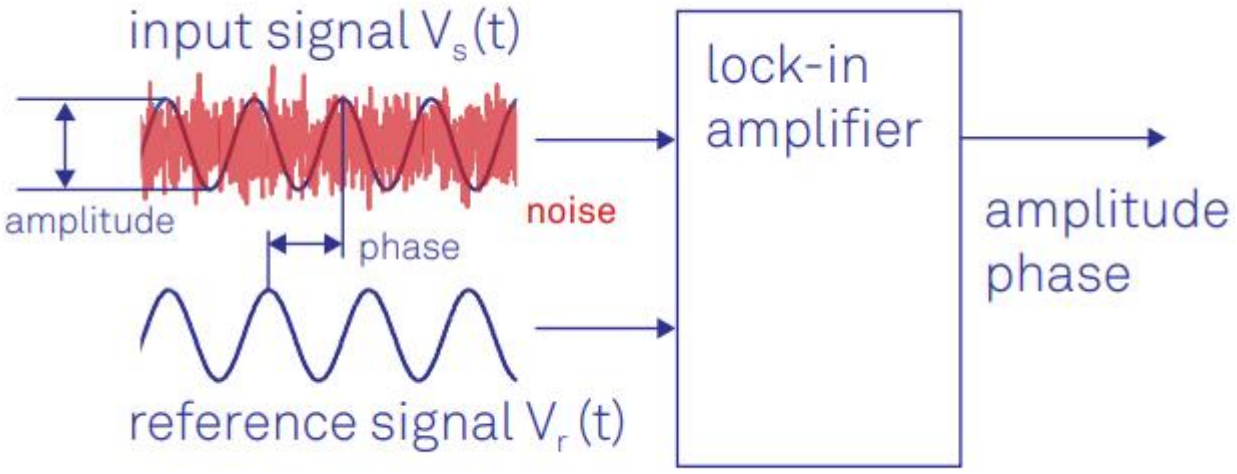

How does lock-in amplifier measure?

Signal amplitude and phase

Demodulation

$V_s(t) = \boldsymbol{V_s} \sin(\omega_s t + \boldsymbol{\phi_s})$

$\omega_s = 2\pi f_s$

$V_s(t) \otimes V_r(t)$

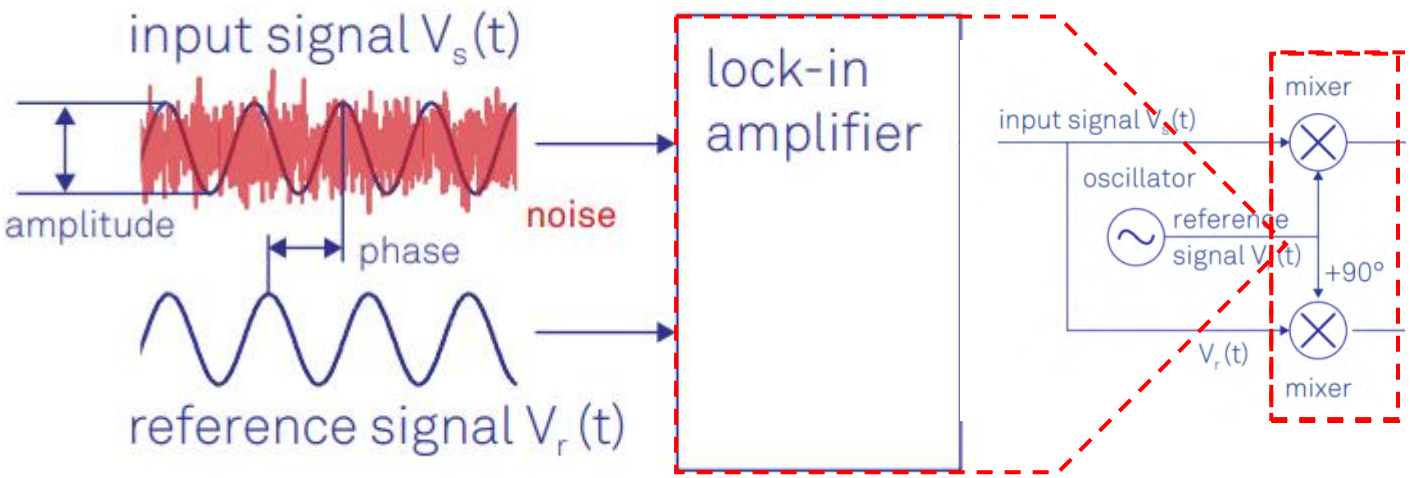

$\frac{\boldsymbol{V_s}}{2} \cos(\boldsymbol{\phi_s}) = x$

$\frac{\boldsymbol{V_s}}{2} \sin(\boldsymbol{\phi_s}) = y$

$V_r(t)$

$= V_r \cos(\omega_r t + \phi_r)$

$\omega_r = 2\pi f_r$

Time constant and filter bandwidth

$\tau_C = 1/2\pi f_{-3dB}$

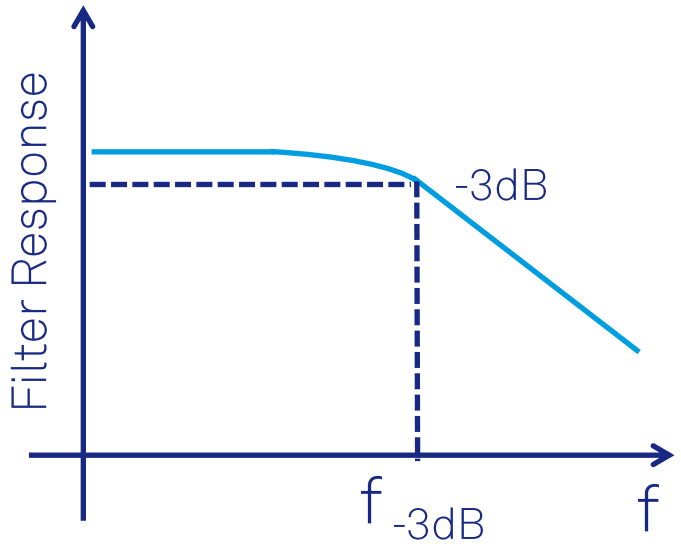

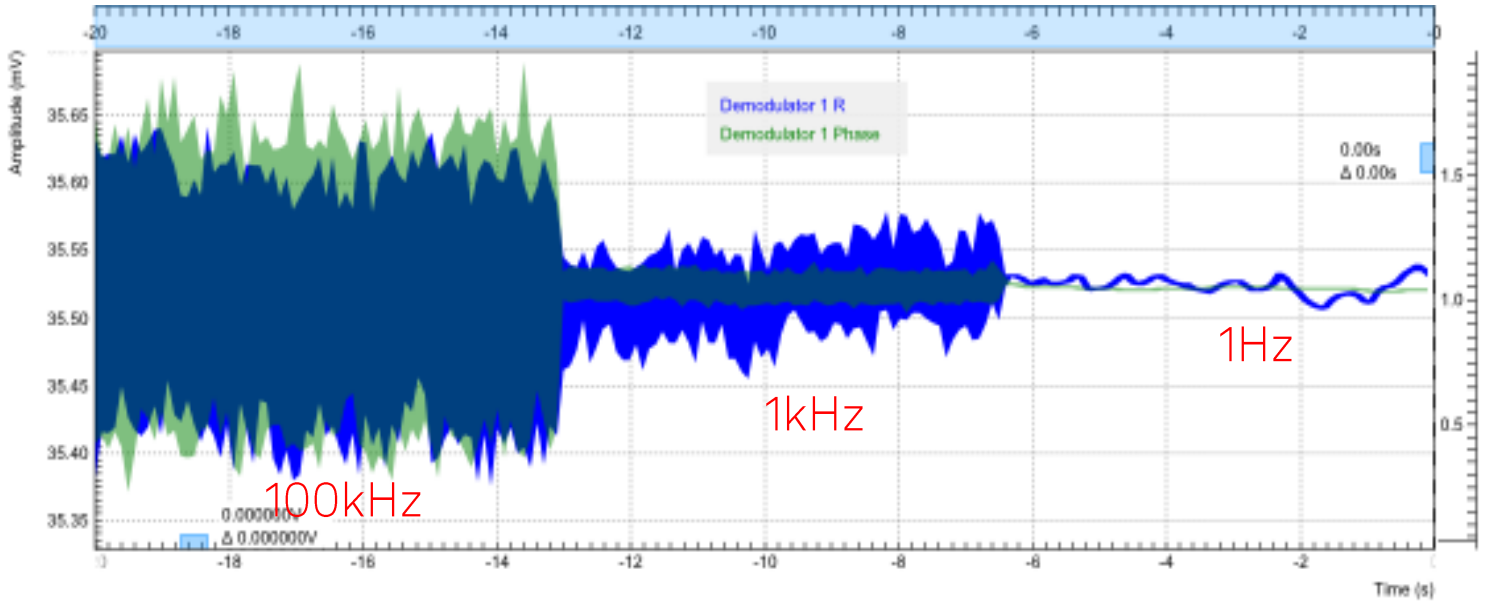

Reducing filter BW → increase time constant
Slower measurements → less noise

Filter settling time

Higher filter orders

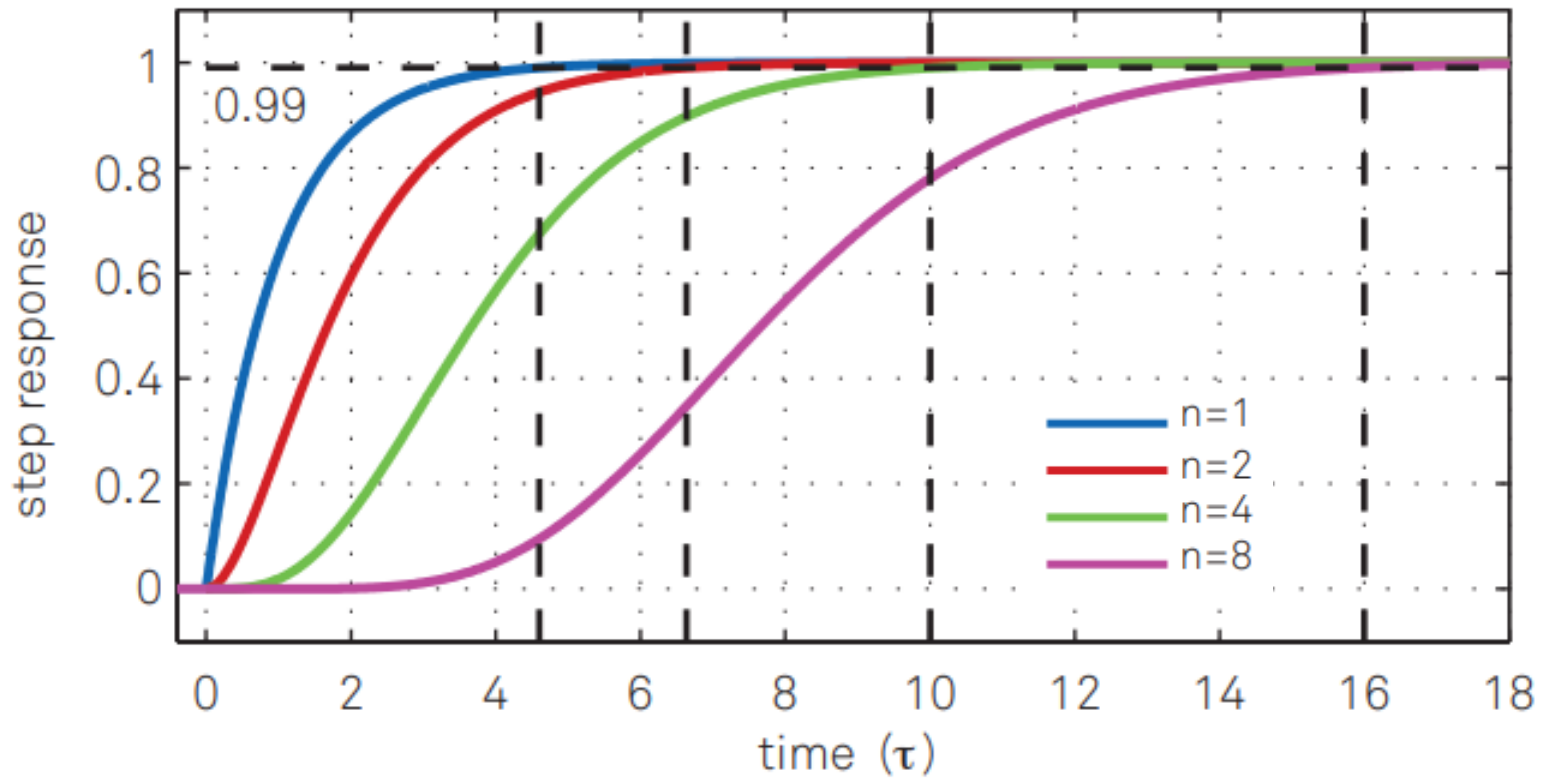

The higher the filter order, the longer it takes for the filter to settle.
Early data sampling leads to erroneous results.

Instrument related noise

The lower the better

Input noise

→ The sum of all the noise sources internal to the instrument, referenced to the signal input

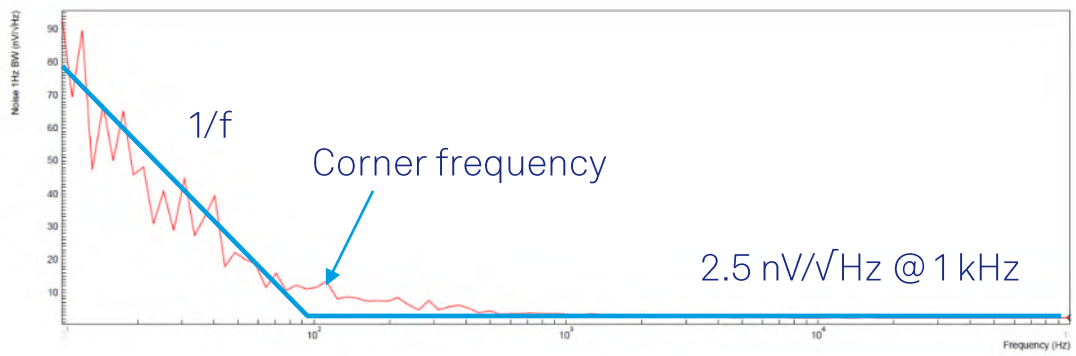

MFLI Input noise density as a function of frequency

Noise dissipated from input ports

→ Noise dissipated from input ports can be absorbed by the system resulting in an increased electronic temperature

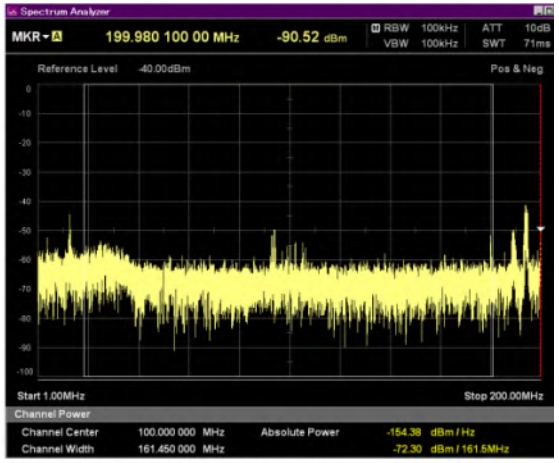

Dissipated noise from MFLI voltage input in the frequency range 10 MHz – 200 MHz

MFLI basic unit

- 1 dual-phase demodulator
- 1 external reference
- Single frequency measurement
- Choice between V or I measurement

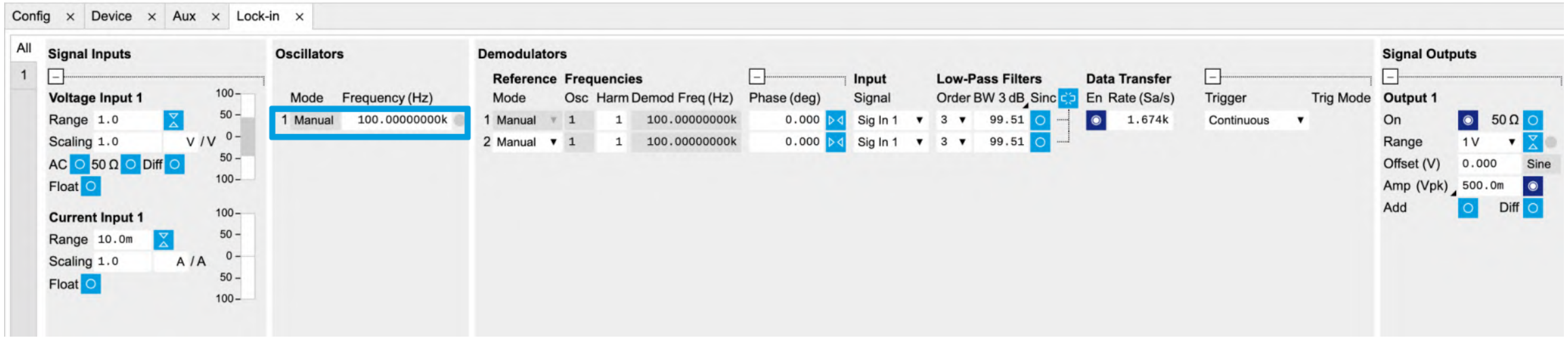

MFLI with MF-MD Multi-demodulator Option

- 4 dual-phase demodulators
- 2 external references
- Simultaneous measurements at 4 different frequencies
- Simultaneous measurements of 3 higher harmonics
- Simultaneous V and I measurements

MFLI with MF-MD Multi-demodulator Option

- 4 dual-phase demodulators
- 2 external references
- Simultaneous measurements at 4 different frequencies
- Simultaneous measurements of 3 higher harmonics
- Simultaneous V and I measurements

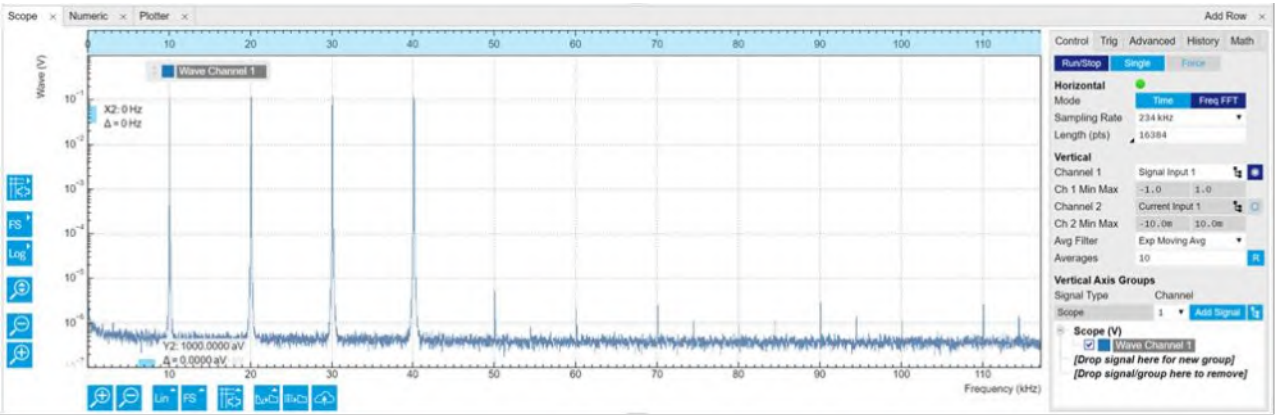

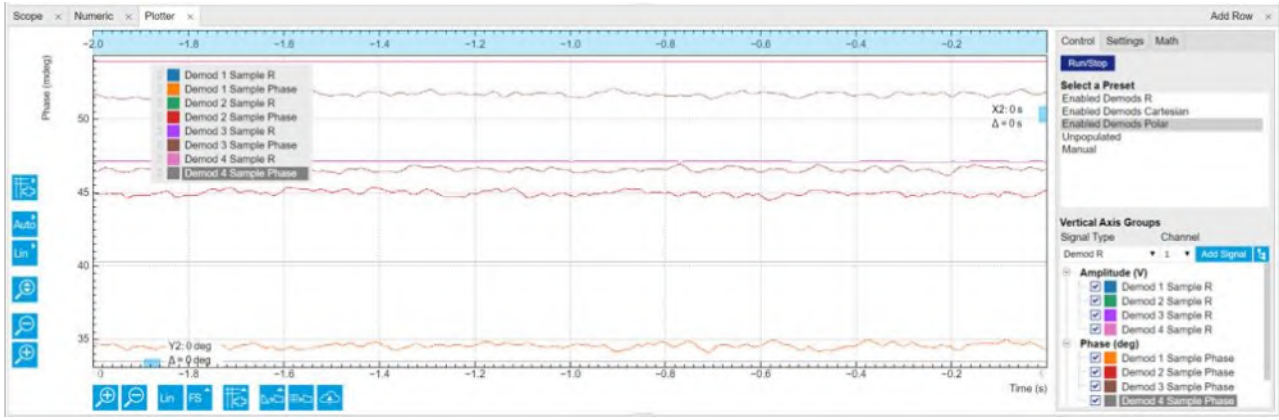

MFLI with MD Multi-demodulator Option

- 4 dual-phase demodulators
- 2 external references
- Simultaneous measurements at 4 different frequencies
- Simultaneous measurements of 3 higher harmonics
- Simultaneous V and I measurements

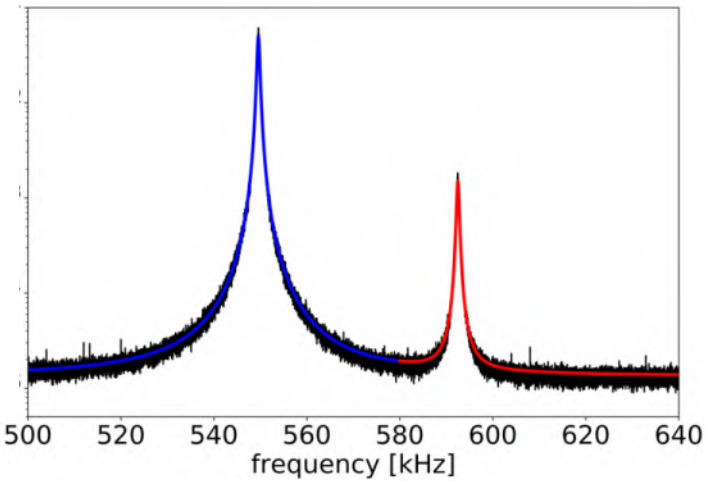

Magnetic nanowire sensing, Poggio Lab, Image

Sensor control and readout

Resonance amplitude and phase characterization

- Frequency sweep
- Determine resonator characteristics
- Use the phase at the resonance as a set point for the phase-locked loop (PLL)

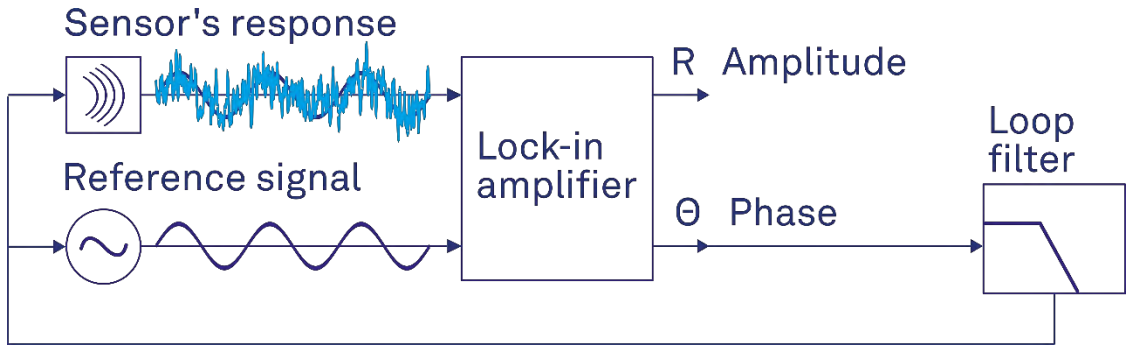

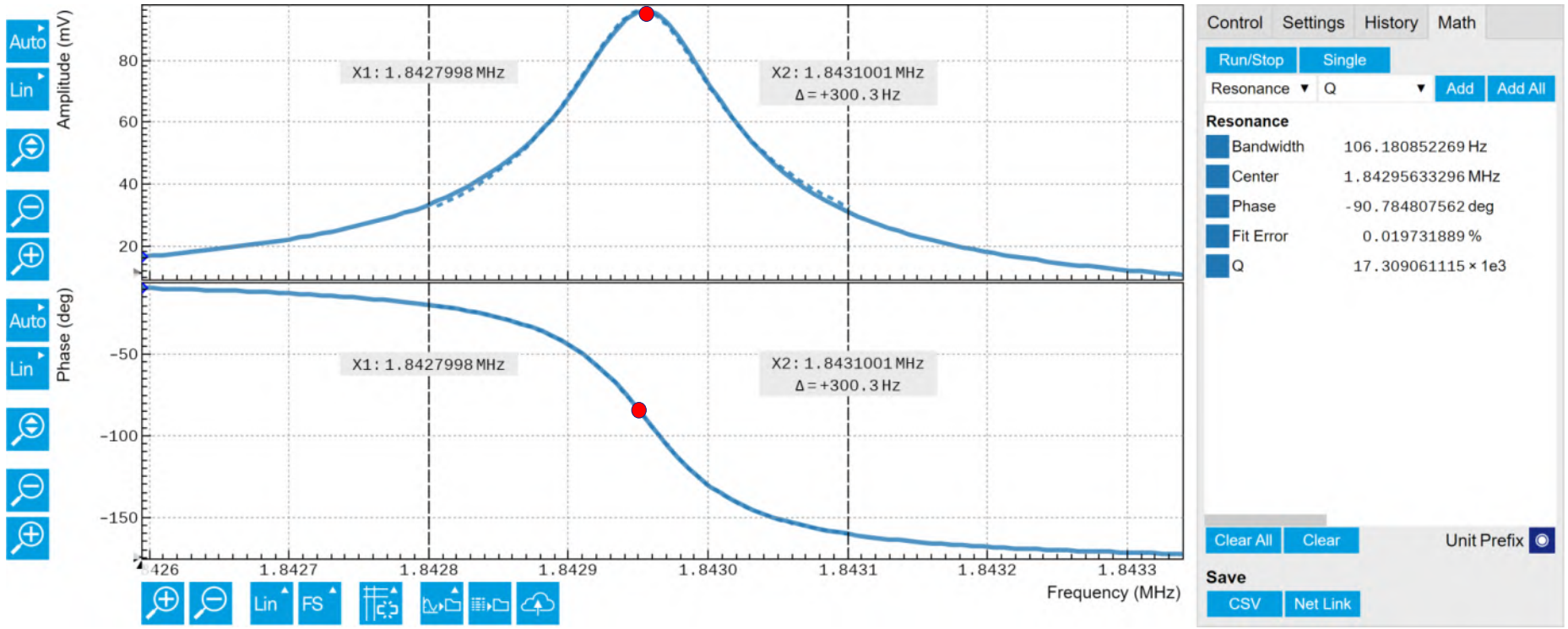

Feedback control loops with MF-PID and MF-MD options

Dual phase-locked loop (PLL)

- The lock-in measures 2 amplitudes and 2 phases
- Compares with setpoints and generates the error signal
- PLL controller adjusts the numerical oscillator frequency to minimize the error
- The frequency shift corresponds to the external magnetic field component

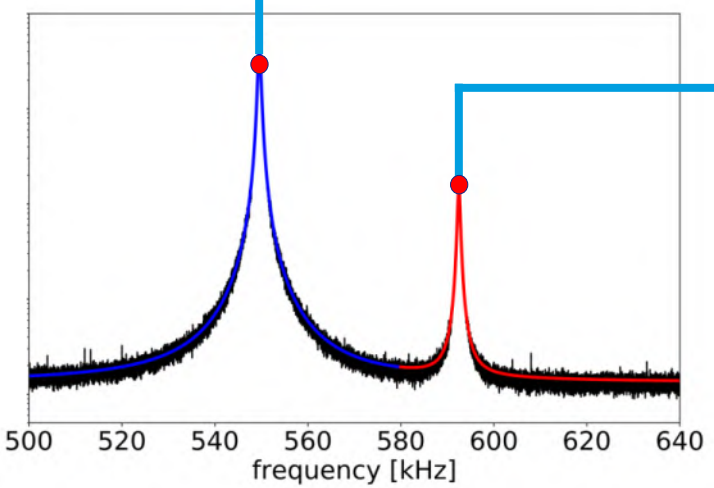

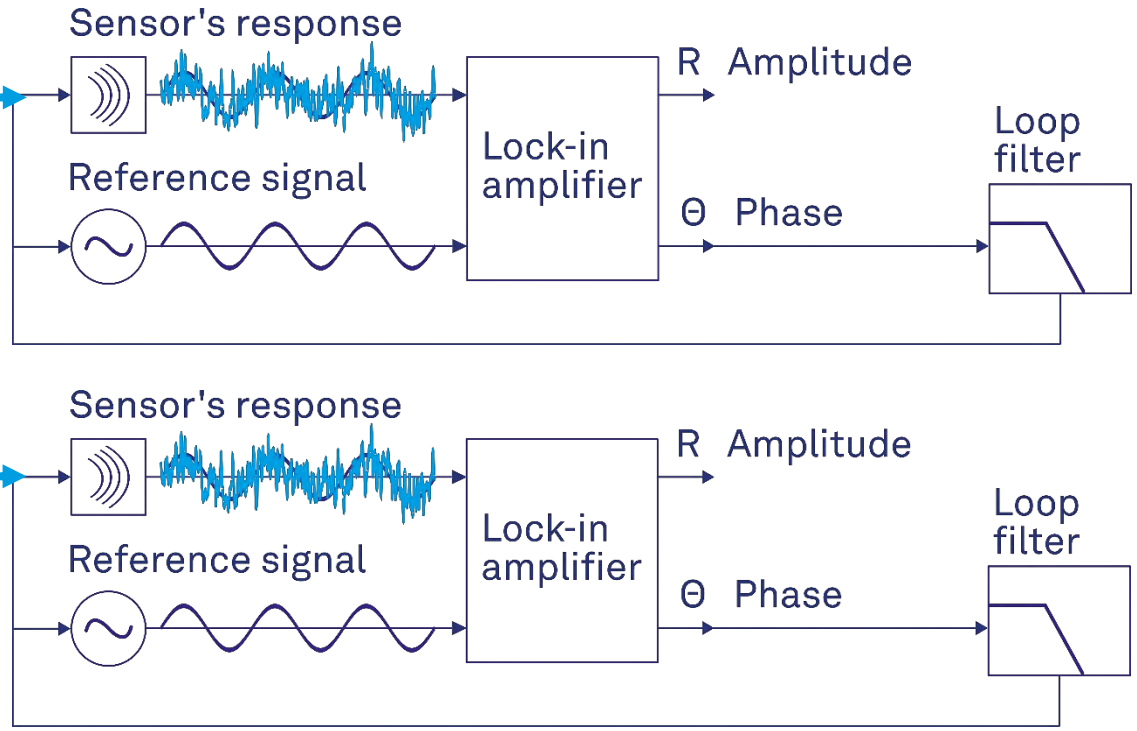

Magnetic sensors characterization and control

All in one.

Your benefits

- Simplify your setup with a single instrument for concurrent characterization and control
- Measure multiple signals simultaneously with the MF-MD Option
- Track and control multiple resonances simultaneously with the MF-PID Option

Outline

- Scanning SQUID microscopy
  - SQUID-on-tip sensors
  - Magnetic imaging with SQUID-on-tip

- Zurich Instruments lock-in amplifiers
  - Measurement principle
  - Multiple mode measurement and control

- Magnetic force microscopy
  - Scaling down the sensor
  - NW MFM

- Comparison between techniques
  - Which sensor for which application?
  - Prospects for improvement

Magnetic imaging by "force microscopy" with 1000 Å resolution

Y. Martin and H. K. Wickramasinghe
IBM T. J. Watson Research Center, P. O. Box 218, Yorktown Heights, New York 10598

(Received 19 December 1986; accepted for publication 19 March 1987)

We describe a new method for imaging magnetic fields with 1000 Å resolution. The technique is based on using a force microscope to measure the magnetic force between a magnetized tip and the scanned surface. The method shows promise for the high-resolution mapping of both static and dynamic magnetic fields.

Appl. Phys. Lett. **50** (20), 18 May 1987

Magnetic force microscopy: General principles and application to longitudinal recording media

D. Rugar, H. J. Mamin, P. Guethner,[a] S. E. Lambert,[b] J. E. Stern,[c] I. McFadyen,[b] and T. Yogi[b]
IBM Research Division, Almaden Research Center, 650 Harry Road, San Jose, California 95120-6099

(Received 15 January 1990; accepted for publication 13 April 1990)

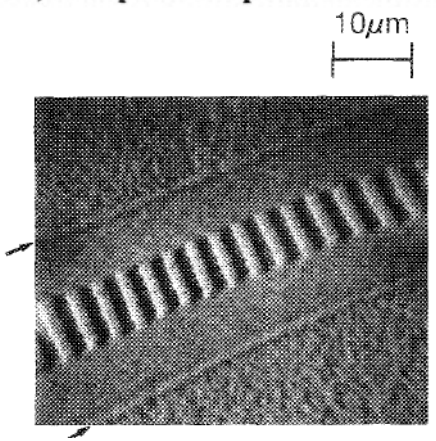

J. Appl. Phys. **68** (3), 1 August 1990

MFM achieves down to 10 nm resolution

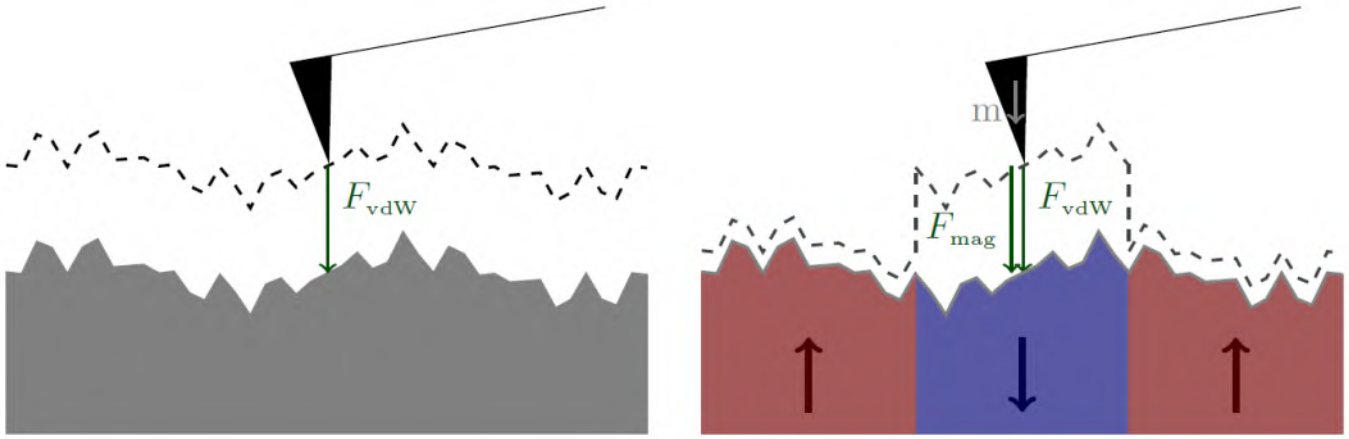

Schwenk, *Ph.D. Thesis in Physics,* University of Basel (2016).

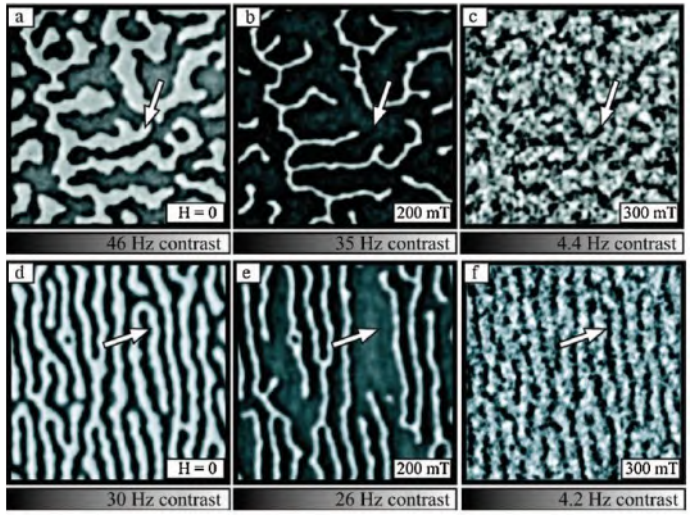

Schmid et al., *Phys. Rev. Lett.* **105**, 197201 (2010).

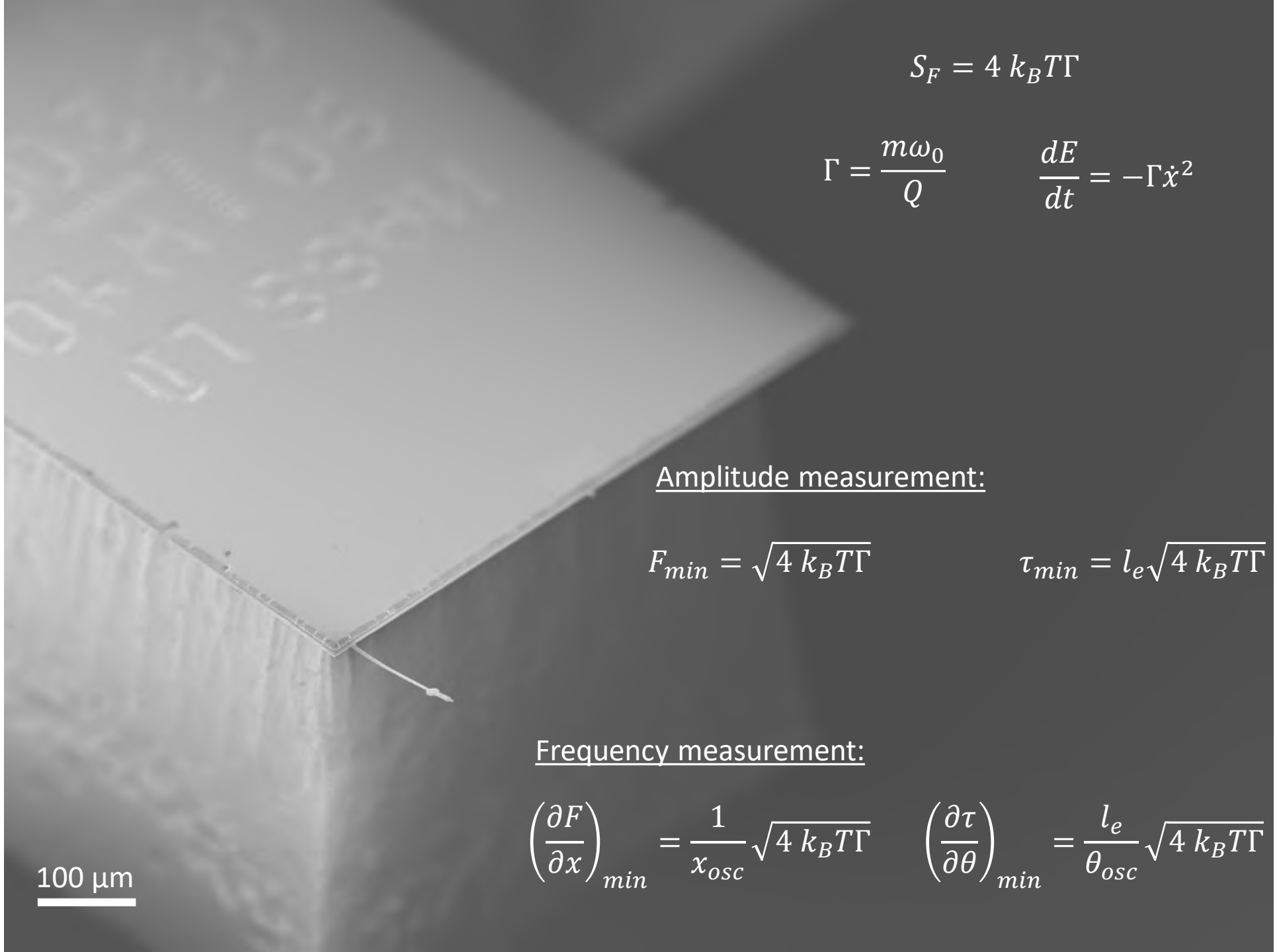

$$S_F = 4\,k_B T\Gamma$$

$$\Gamma = \frac{m\omega_0}{Q} \qquad \frac{dE}{dt} = -\Gamma\dot{x}^2$$

Amplitude measurement:

$$F_{min} = \sqrt{4\,k_B T\Gamma} \qquad \tau_{min} = l_e\sqrt{4\,k_B T\Gamma}$$

Frequency measurement:

$$\left(\frac{\partial F}{\partial x}\right)_{min} = \frac{1}{x_{osc}}\sqrt{4\,k_B T\Gamma} \qquad \left(\frac{\partial \tau}{\partial \theta}\right)_{min} = \frac{l_e}{\theta_{osc}}\sqrt{4\,k_B T\Gamma}$$

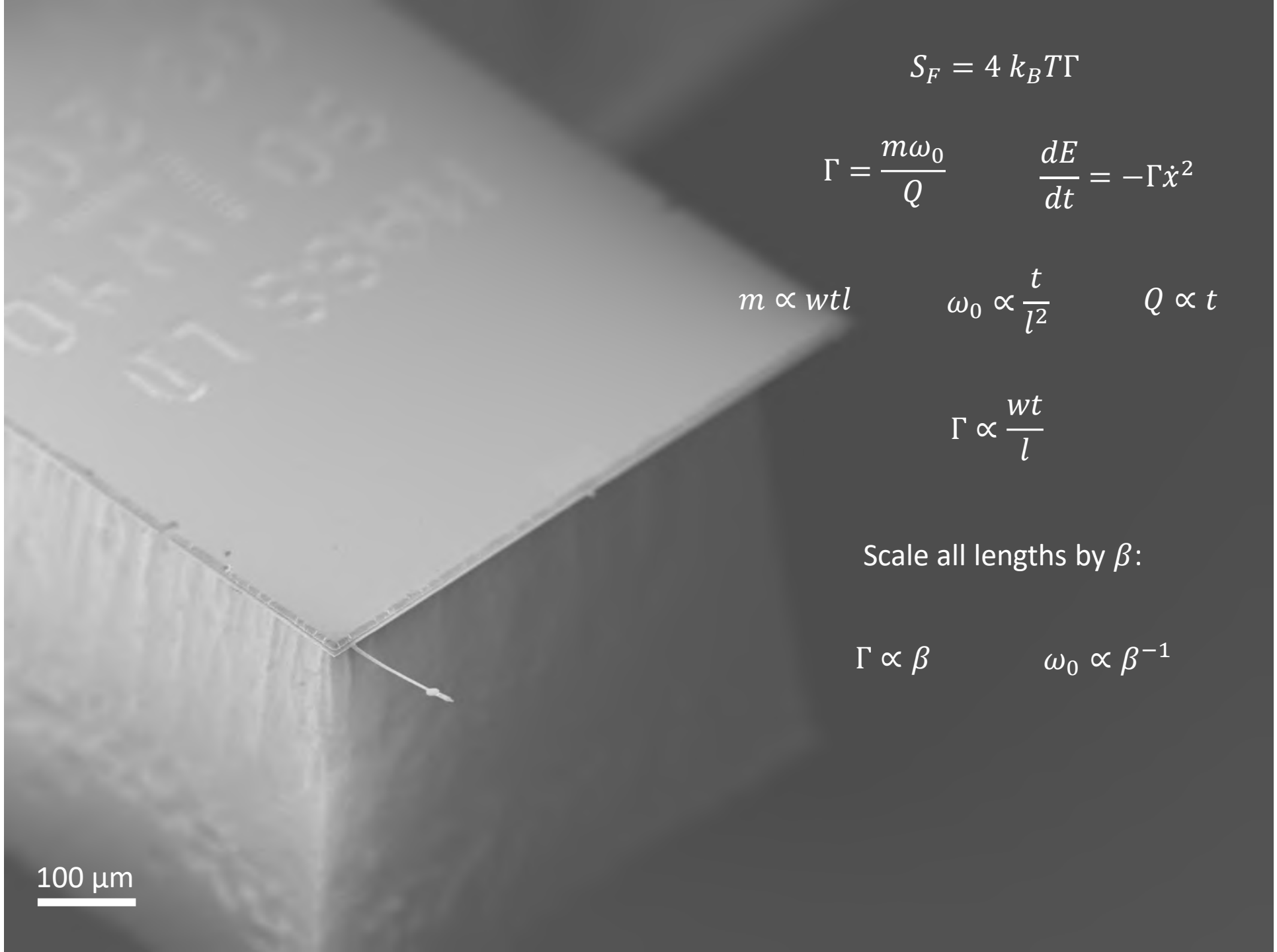

$$S_F = 4\,k_B T \Gamma$$

$$\Gamma = \frac{m\omega_0}{Q} \qquad \frac{dE}{dt} = -\Gamma \dot{x}^2$$

$$m \propto wtl \qquad \omega_0 \propto \frac{t}{l^2} \qquad Q \propto t$$

$$\Gamma \propto \frac{wt}{l}$$

Scale all lengths by β:

$$\Gamma \propto \beta \qquad \omega_0 \propto \beta^{-1}$$

‘Bottom-up’ scanning force sensors

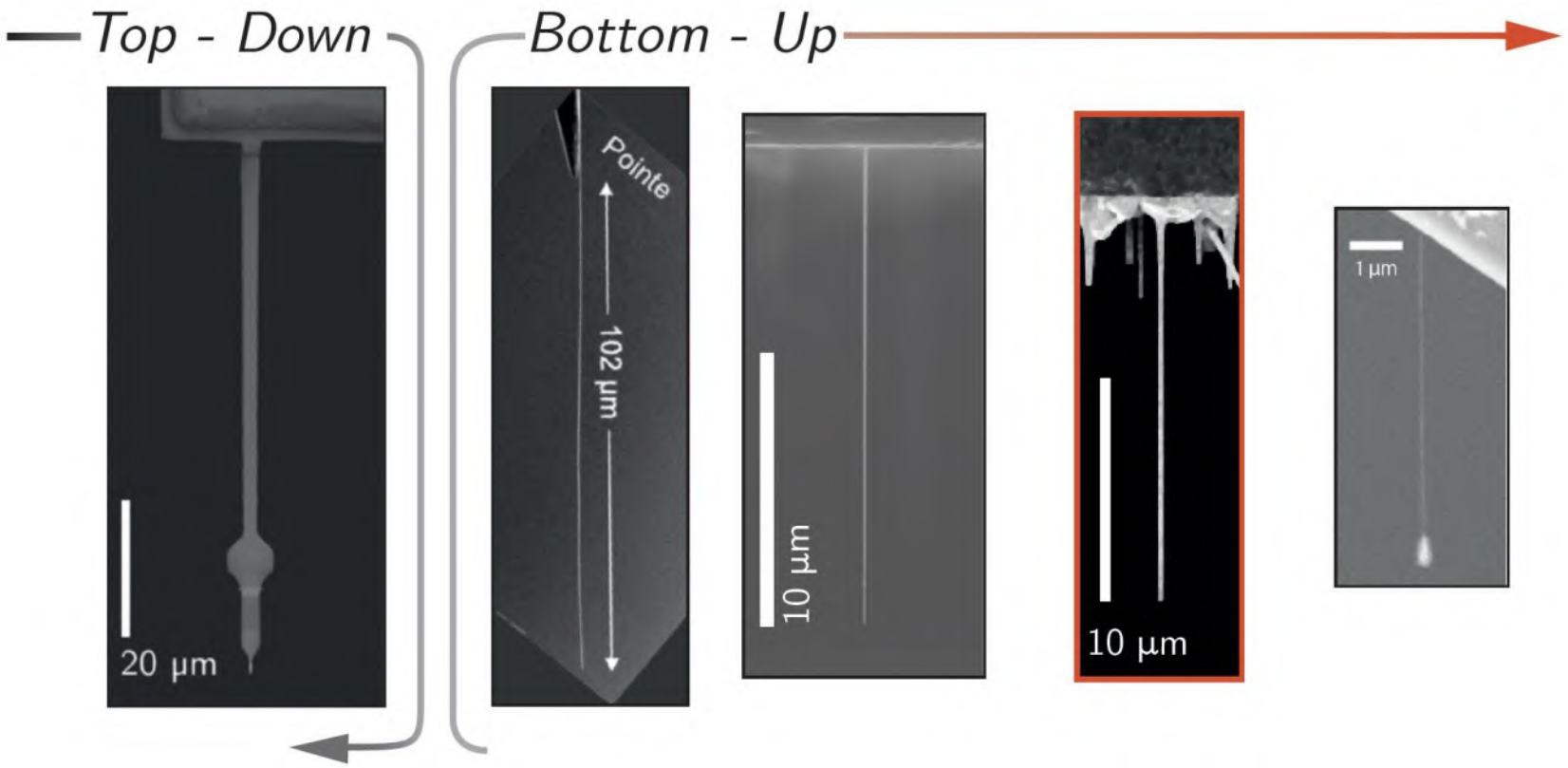

Rossi, *Ph.D. Thesis in Physics,* University of Basel (2019).

NW Cantilevers

Table 1. Experimentally determined parameters of singly-clamped NW cantilevers. Here the diameter d is the average cross-sectional width and $\omega_0/2\pi$ is the average frequency of the fundamental flexural mode doublet. The quality factor Q is the average value of the fundamental flexural mode doublet, taken for a freestanding NW, far from any sample surface and measured at low ambient pressures. RT stands for room temperature.

Material	Cross-section	d (nm)	L (μm)	$\omega_0/2\pi$ (kHz)	k (N m^{-1})	Q	Reference
GaAs/AlGaAs	Hexagonal	350	25	417	1×10^{-2}	50 000 (4 K)	[9, 10]
GaAs	Hexagonal	234	16.8	598	8.3×10^{-3}	46 553 (4 K)	[11]
GaAs	Hexagonal	100	<25	1197	8.3×10^{-3}	4900 (RT)	[12]
GaAs/AlGaAs	Hexagonal	390	20	795	9×10^{-2}	6700 (4K)	[13]
GaAs	Hexagonal	130	14.5	465	—	2000–3000 (RT)	[14]
InAs	Hexagonal	60–80	4–5.5	2023.9	3.6×10^{-3}	1752 (RT)	[15]
SiC	Circular	150	52	113	4×10^{-4}	2890 (RT)	[1]
SiC	Circular	200	50	78	1.5×10^{-4}	1000 (RT)	[16]
SiC	Circular	120	165	6.7	3×10^{-6}	3000 (RT)	[17]
SiC	Circular	284	128	33	—	36 000 (RT)	[18]
SiC	Circular	206	93	43	—	159 000 (RT)	[18]
SiC	Circular	50	7	1519	—	2500 (RT)	[19]
SiC	Circular	300	6	6140	1.5	33 (RT, Air)	[20]
Si	Circular	44	14.4	210.5	2.8×10^{-5}	9250 (RT)	[21]
Si	Circular	46	12.9	273	6.6×10^{-5}	7250 (RT)	[21]
Si	—	35	15	1060	6.5×10^{-4}	25 000 (8 K)	[6]
Si	—	50	15	333	1.5×10^{-4}	18 000 (6 K)	[7]
Si	Circular	50	15	197.5	2.0×10^{-5}	3000–3500 (RT)	[22]
Si	Elongated circular	60, 80	20	342	1×10^{-4}	8150 (4K)	[8]
Si	Hexagonal	100–300	5–10	2000–6000	—	2000 (RT)	[23]
Si	Hexagonal	165	12.7	1772.4	—	3000 (RT)	[24]
Si	Hexagonal	90	9.3	2504.3	—	3000 (RT)	[24]
Si	Hexagonal	100–200	6–8	3500–4000	$2.4 - 5 \times 10^{-2}$	3000–3500 (RT)	[25]
Si	Hexagonal	150 (clamp), 60 (tip)	11.3	2480	—	—	[26]
Si	Hexagonal	39–400	2–20	1000–12 000	—	3000–25 000 (RT)	[27]
Si (metallized)	Hexagonal	142	2.25	200 000	110.3	2000 (25 K)	[28]
Si (metallized)	Hexagonal	118	2.1	188 000	62.9	2500 (25 K)	[28]
Si	Hexagonal	81	1.69	215 000	31.4	5750 (25 K)	[28]
Si	Hexagonal	74	2.77	80 000	6.0	13 100 (25 K)	[28]
CNT	Circular	50	18	270	$\sim 10^{-4}$	250 (RT)	[29]
CNT	Circular	1–3	5	38 178.5	4.5×10^{-8}	2245 (RT)	[30]
CNT	Circular	4	1.2	5955	2.1×10^{-5}	—	[31]
CNT	Circular	—	—	363.5	4.8×10^{-6}	571 (RT)	[31]

Braakman & Poggio, *Nanotechnology* **30**, 332001 (2019).

GaAs NWs

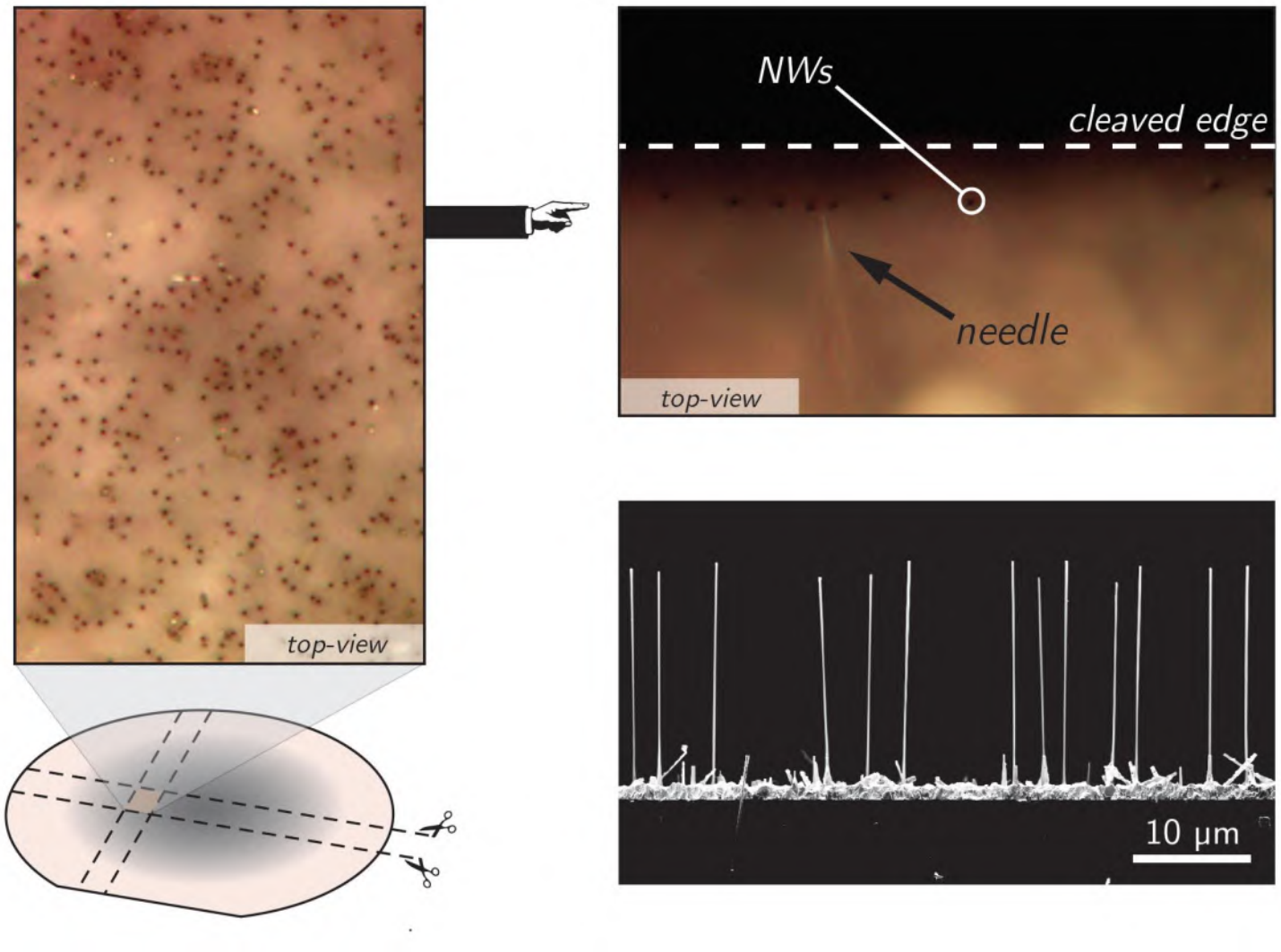

NWs from Fontcuberta group.

NW force microscope

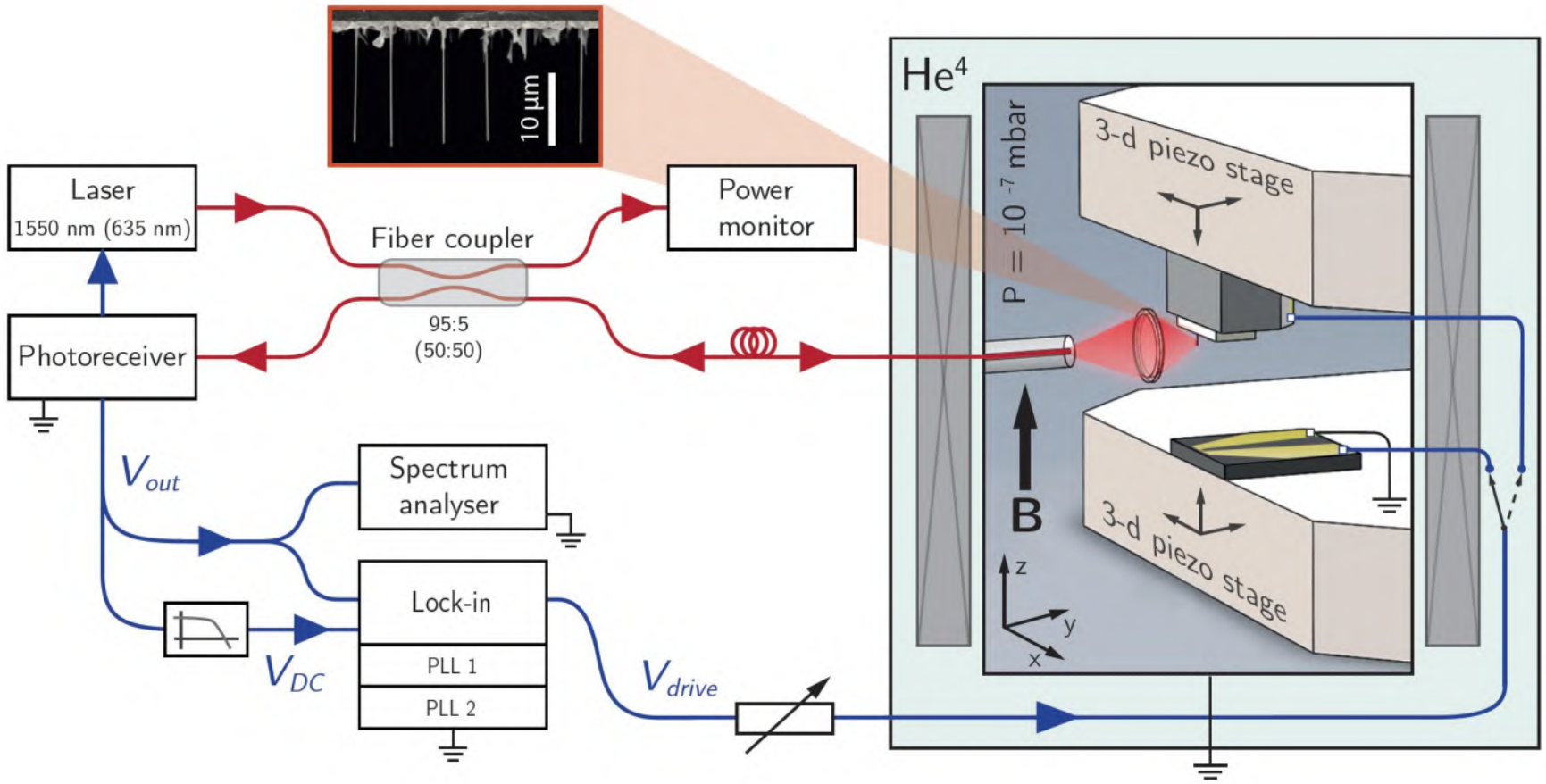

NW force microscope

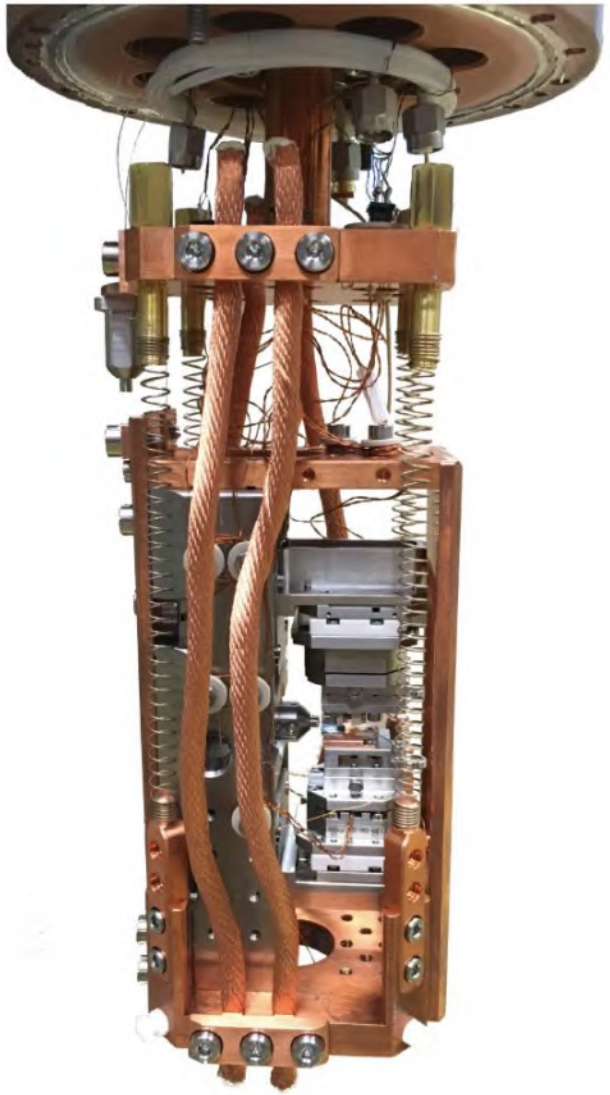

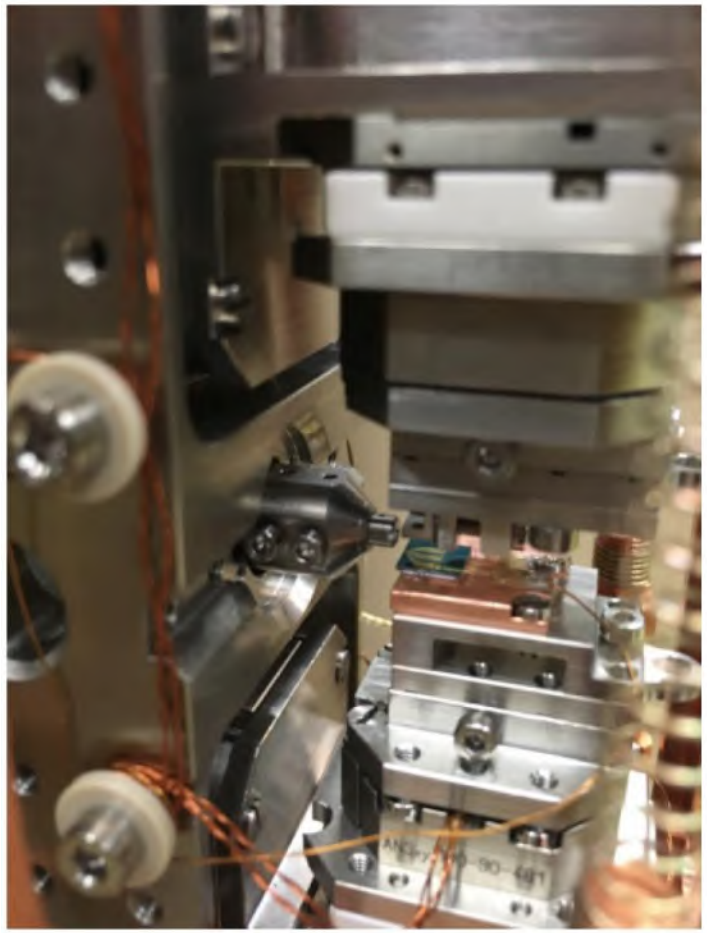

Rossi, *Ph.D. Thesis in Physics,* University of Basel (2019).

Interferometric displacement detection

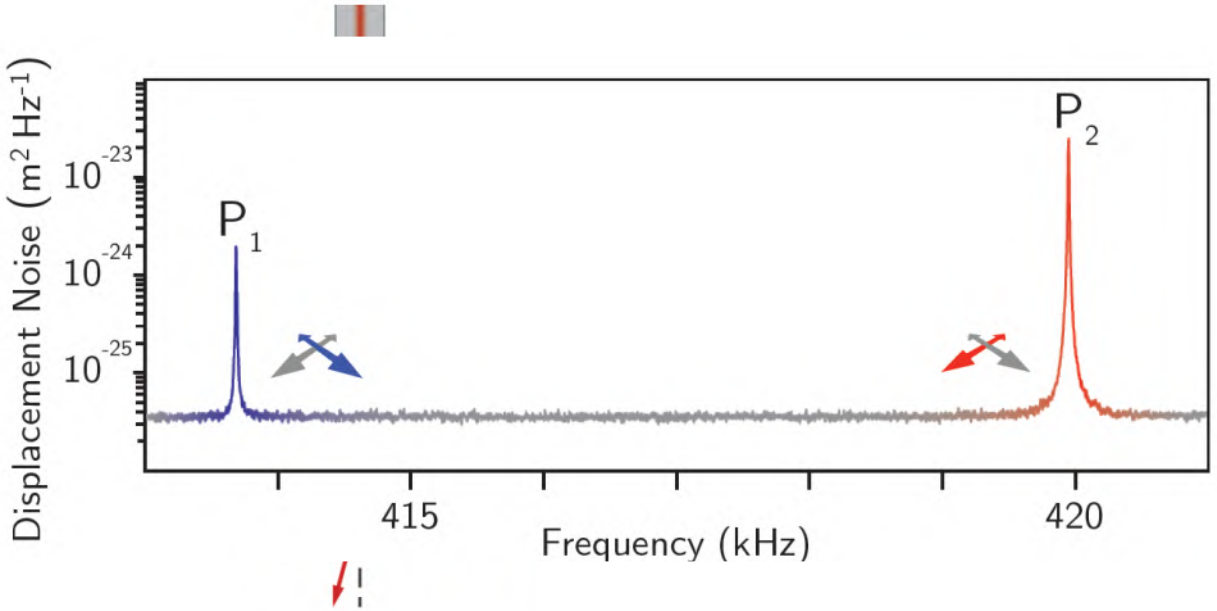

Scanning nanowire microscopy

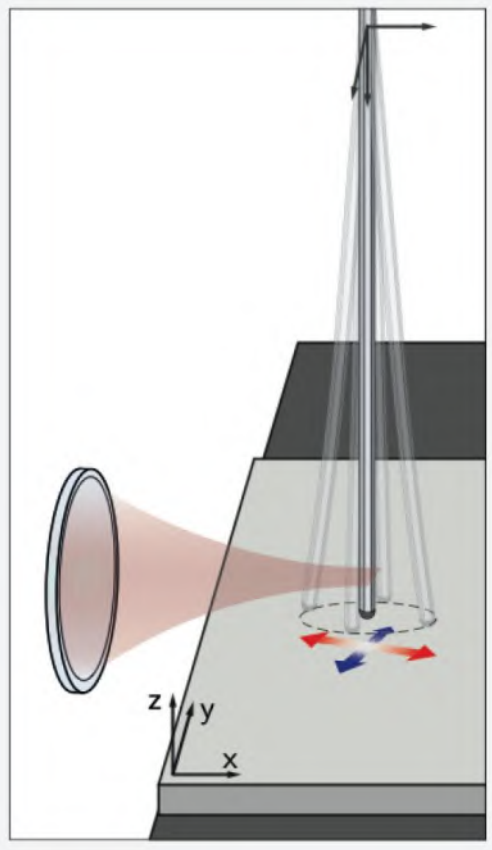

Electrostatic force

- $\mathbf{F}_q = q\mathbf{E}$
- V_{drive} sweep through $f_{1,2}$
- $q_{tot} = 30 \pm 10e$

Dielectric force

- $\mathbf{F}_p = -\nabla(\alpha|\mathbf{E}|^2)$
- V_{drive} sweep through $\frac{f_{1,2}}{2}$
- $\alpha = 10^{-29}\frac{C}{Vm}$

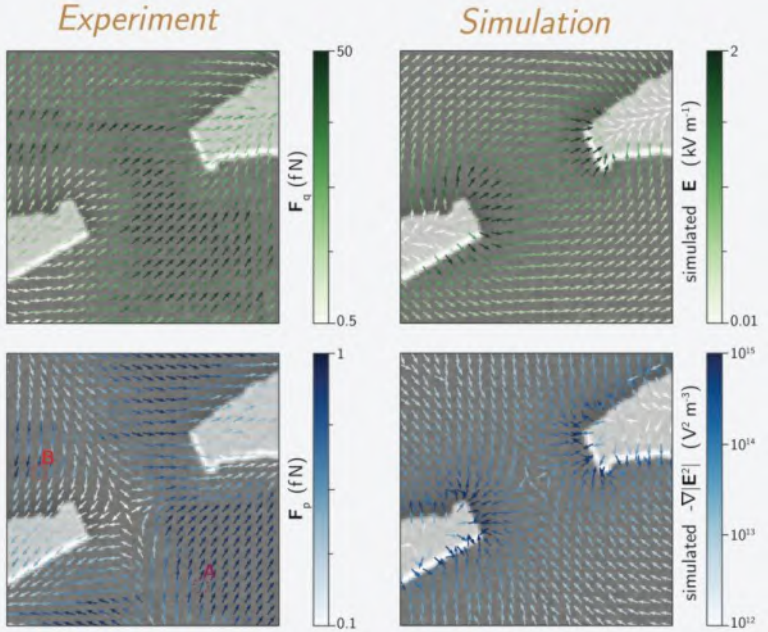

Rossi et al., *Nat. Nanotechnol.* **12**, 150 (2017).

Mercier de Lépinay et al., *Nat. Nanotechnol.* **12**, 156 (2017).

NWs with magnetic tips

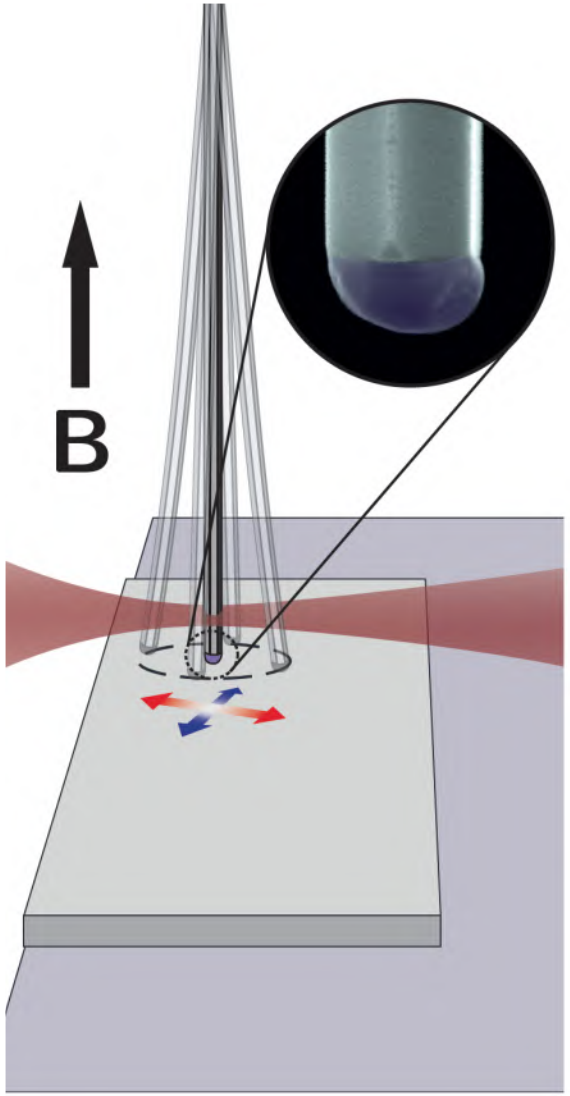

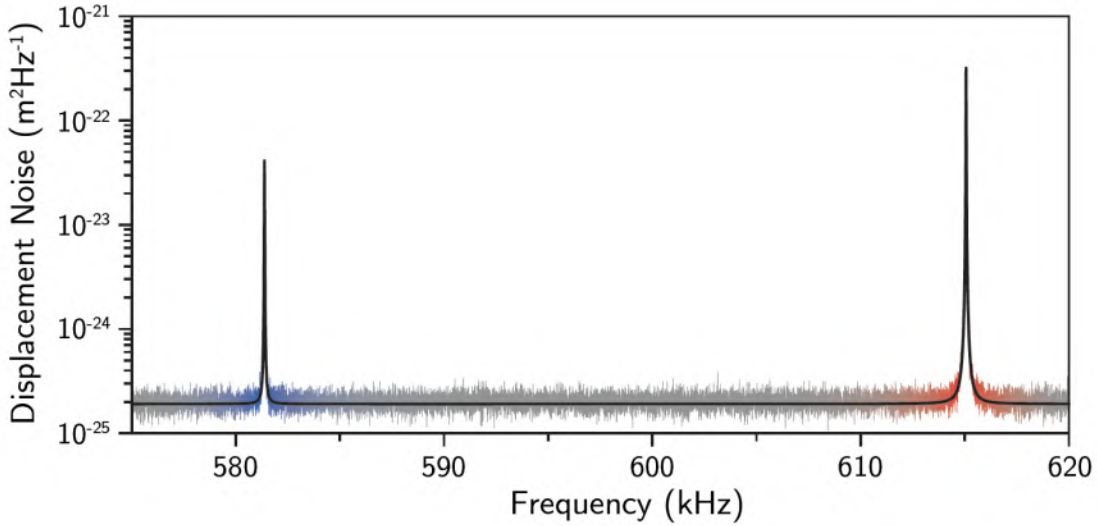

Length $\sim 17 \pm 1\,\mu$m with diameter $\sim 225 \pm 15$ nm

- $f \sim [500 - 700]$ kHz
- $Q \sim [30 - 50] \times 10^3$
- $k \sim [1 - 10]$ mN/m
- $M \sim 700$ fg
- $\Gamma \sim 50 \times 10^{-15}$ kg/s
- $F_{min} \sim 4$ aN/$\sqrt{\text{Hz}}$

Rossi et al., *Nano Lett.* **19**, 930 (2019).

Quantifying sensitivity

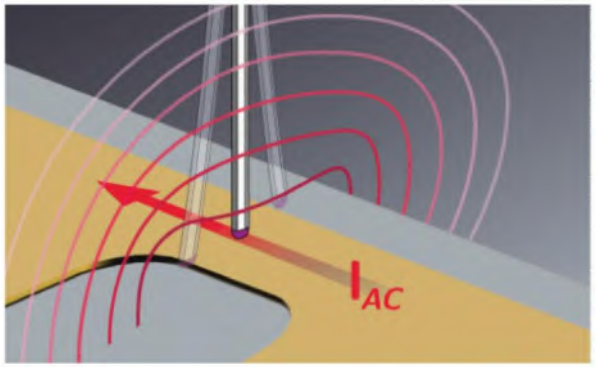

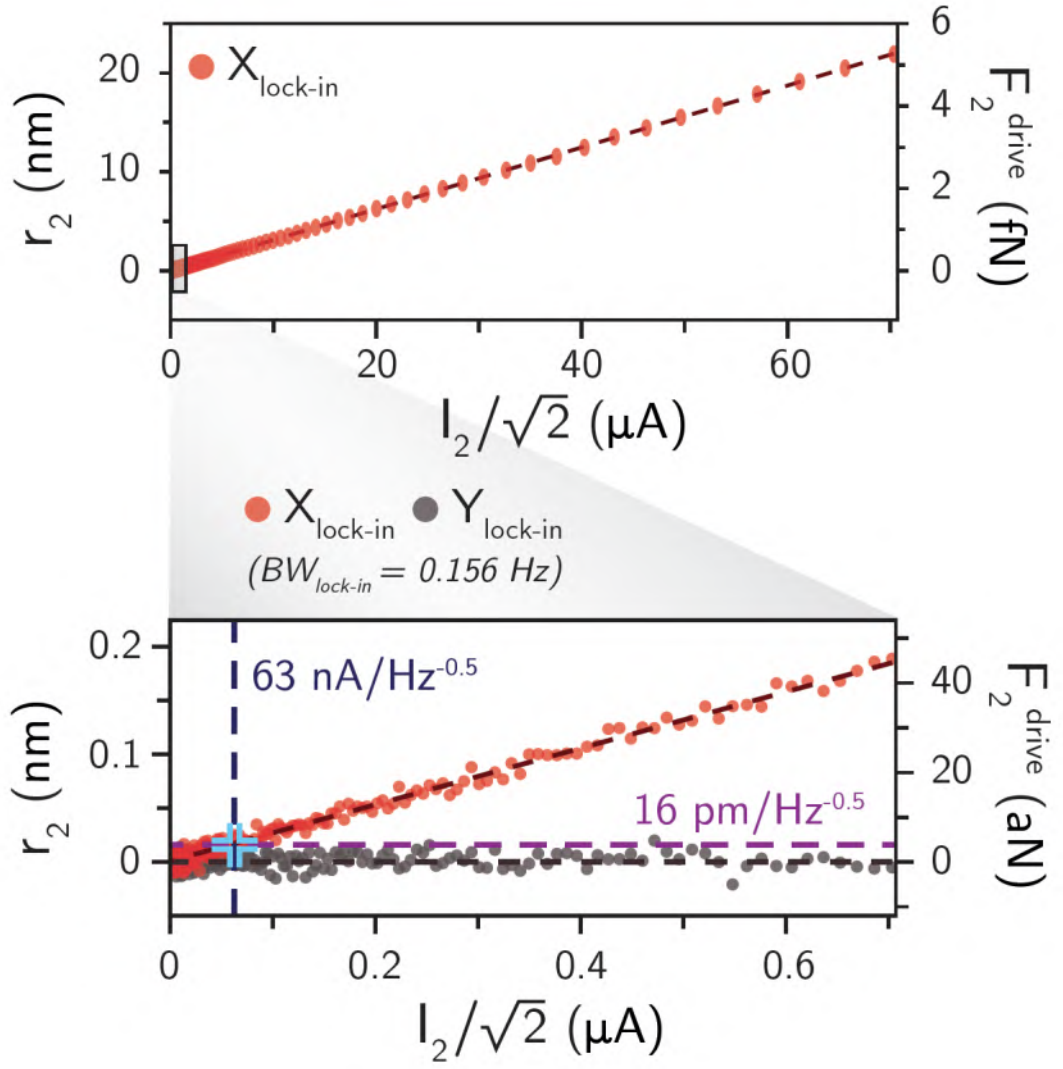

Rossi et al., *Nano Lett.* **19**, 930 (2019).

Quantifying sensitivity

MBE-grown MnAs-tipped NWs

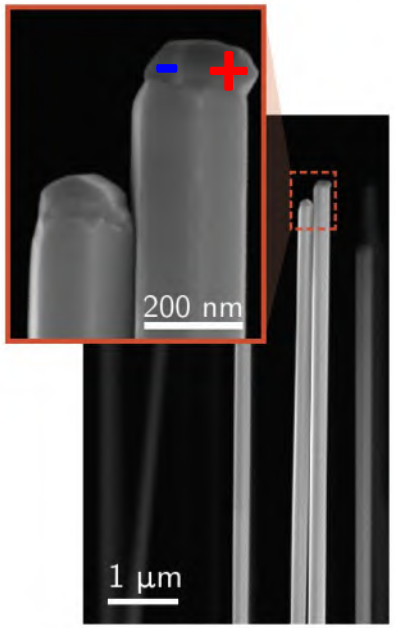

F_{min} = 4 aN/(Hz)$^{1/2}$

At 250 nm spacing:

dB/dx_{min} = 11 mT/m(Hz)$^{1/2}$

FEBID-grown Co NWs

F_{min} = 25 aN/(Hz)$^{1/2}$

At 200 nm spacing:

B_{min} = 3 nT/(Hz)$^{1/2}$

Rossi et al., *Nano Lett.* **19**, 930 (2019).
Mattiat et al., *Phys. Rev. Appl.* **13**, 044043 (2020).

NW MFM

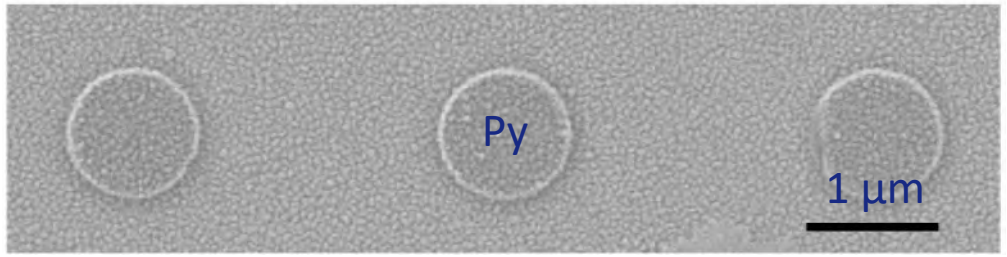

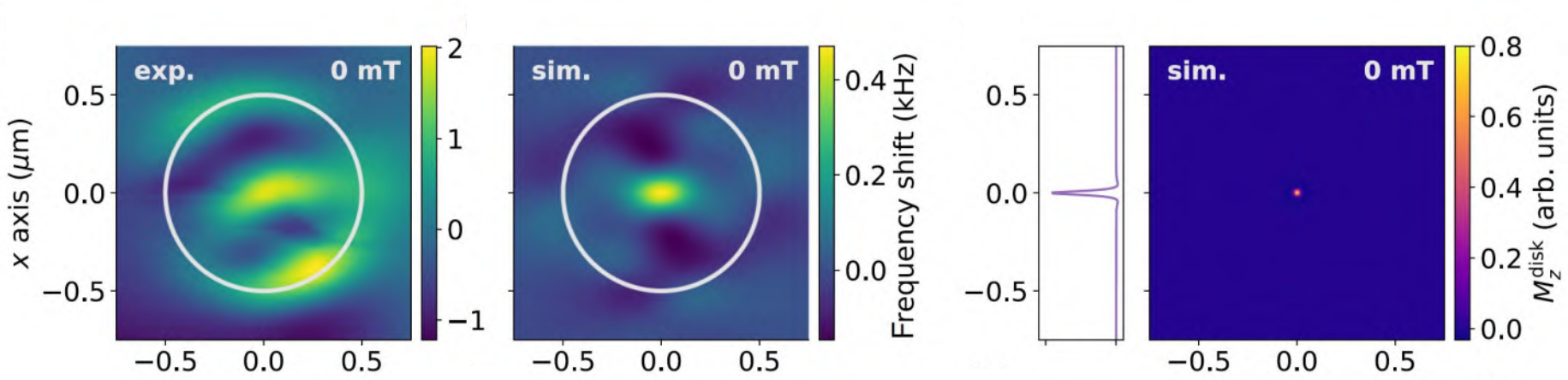

Mattiat et al., *Phys. Rev. Appl.* **13**, 044043 (2020).

Scanning Nitrogen-vacancy Center Microscopy (SNVM)

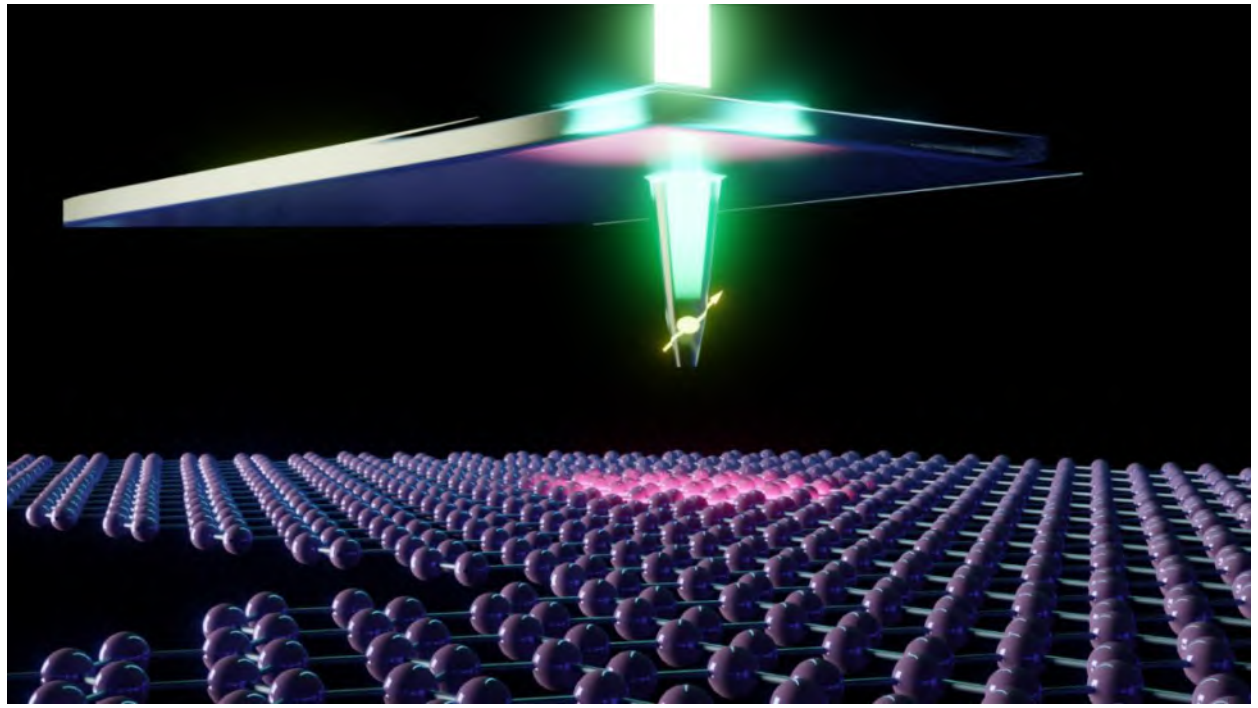

Sensitivity down to
100 nT/(Hz)$^{1/2}$

Spatial resolution
down to 10 nm

Imaging current with SNVM

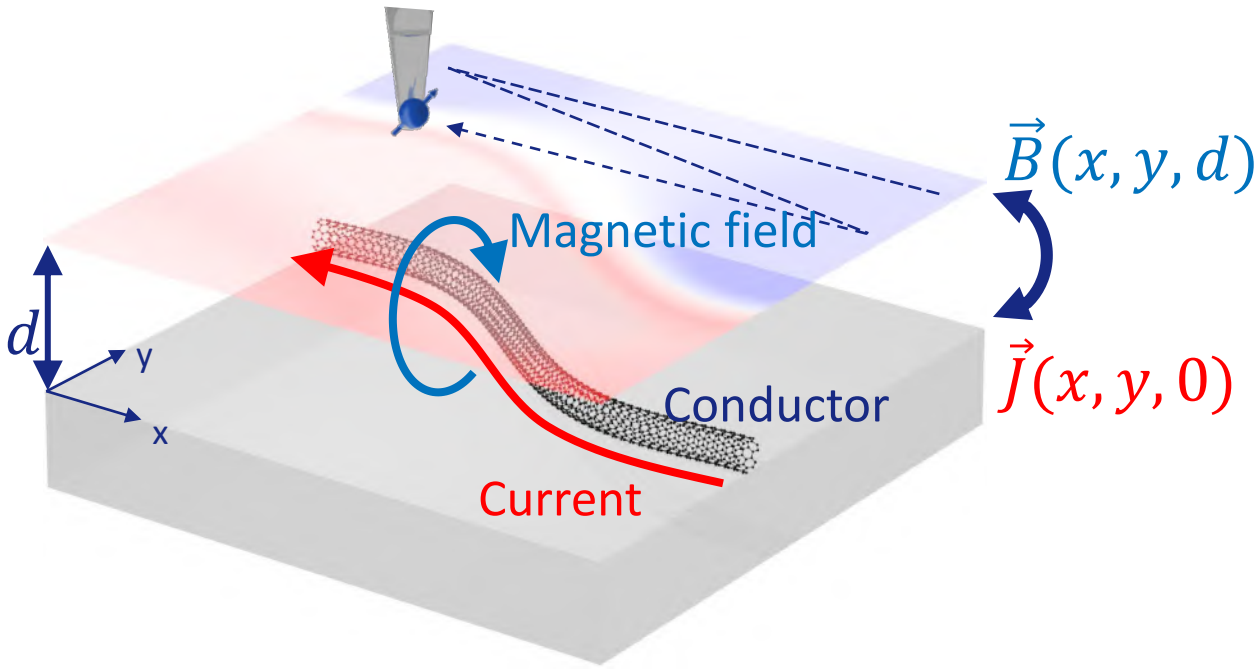

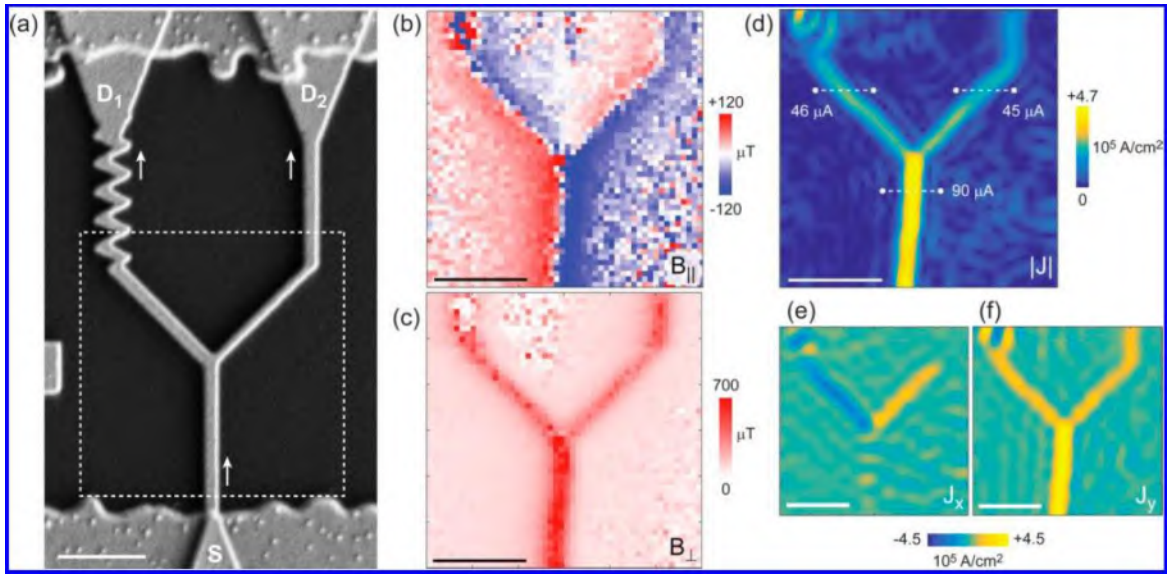

Chang et al., *Nano Lett.* **17**, 2367 (2017).

Scanning NV microscopy of 2D magnets

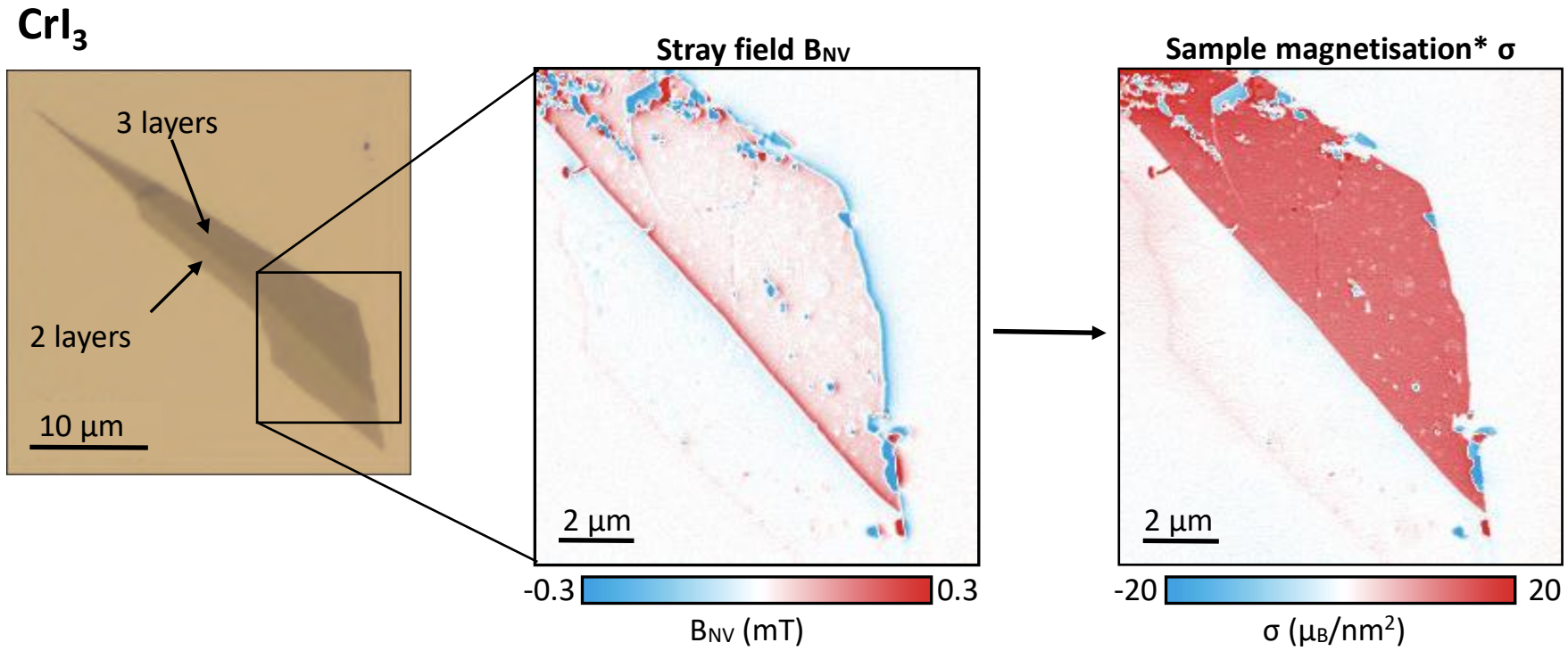

Thiel et al., *Science* **364**, 973 (2019).

Contrast & Techniques

SSM

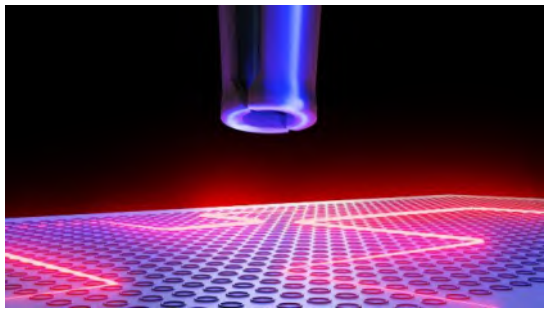

Current density $\vec{J}$

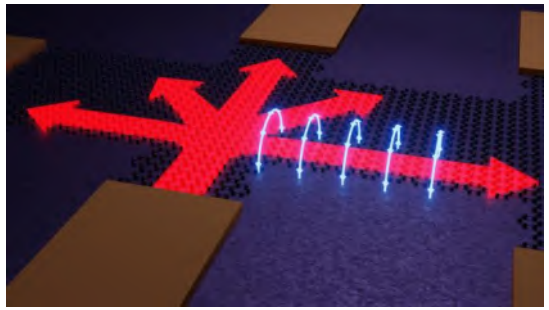

Magnetic flux Φ_z

NW MFM

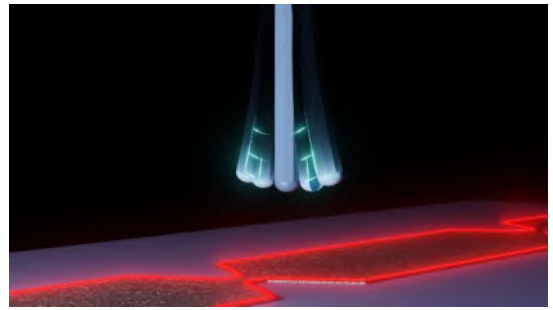

Magnetic field $\vec{B}$

Magnetization $\vec{M}$

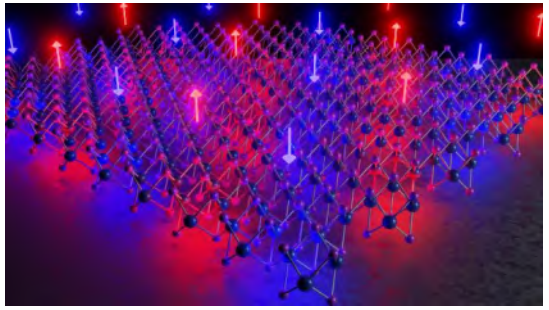

SNVM

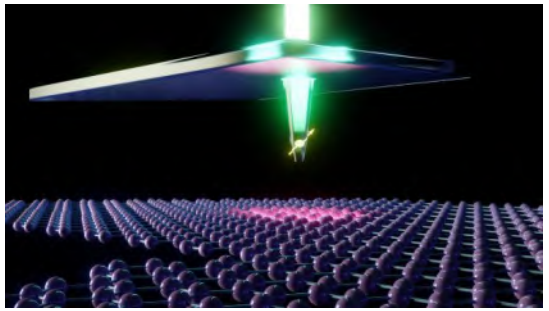

Magnetic field derivative $\frac{\partial B_z}{\partial x}$

Magnetic field component B_z

Sensitivity to Current

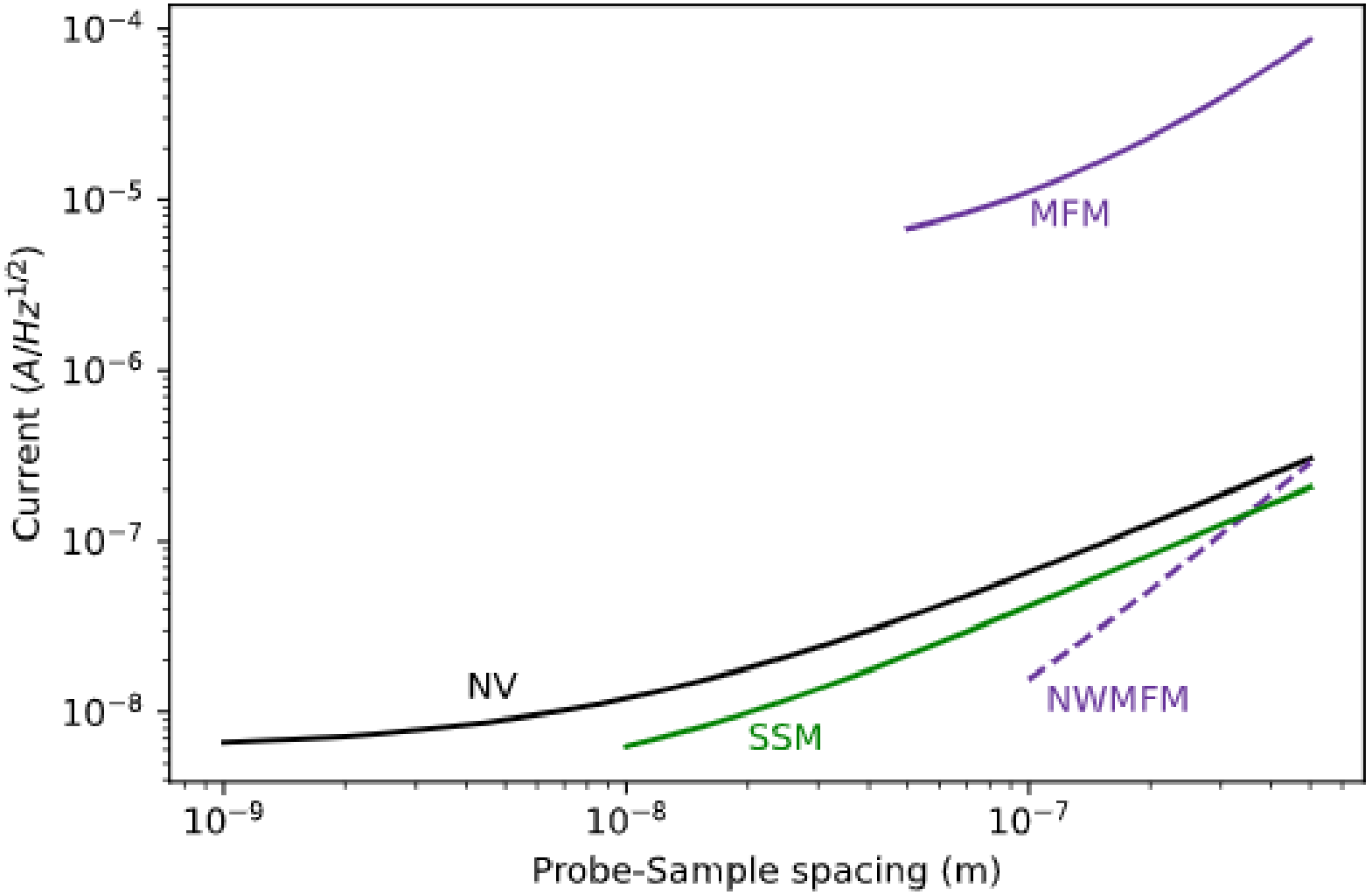

Sensitivity to Magnetization

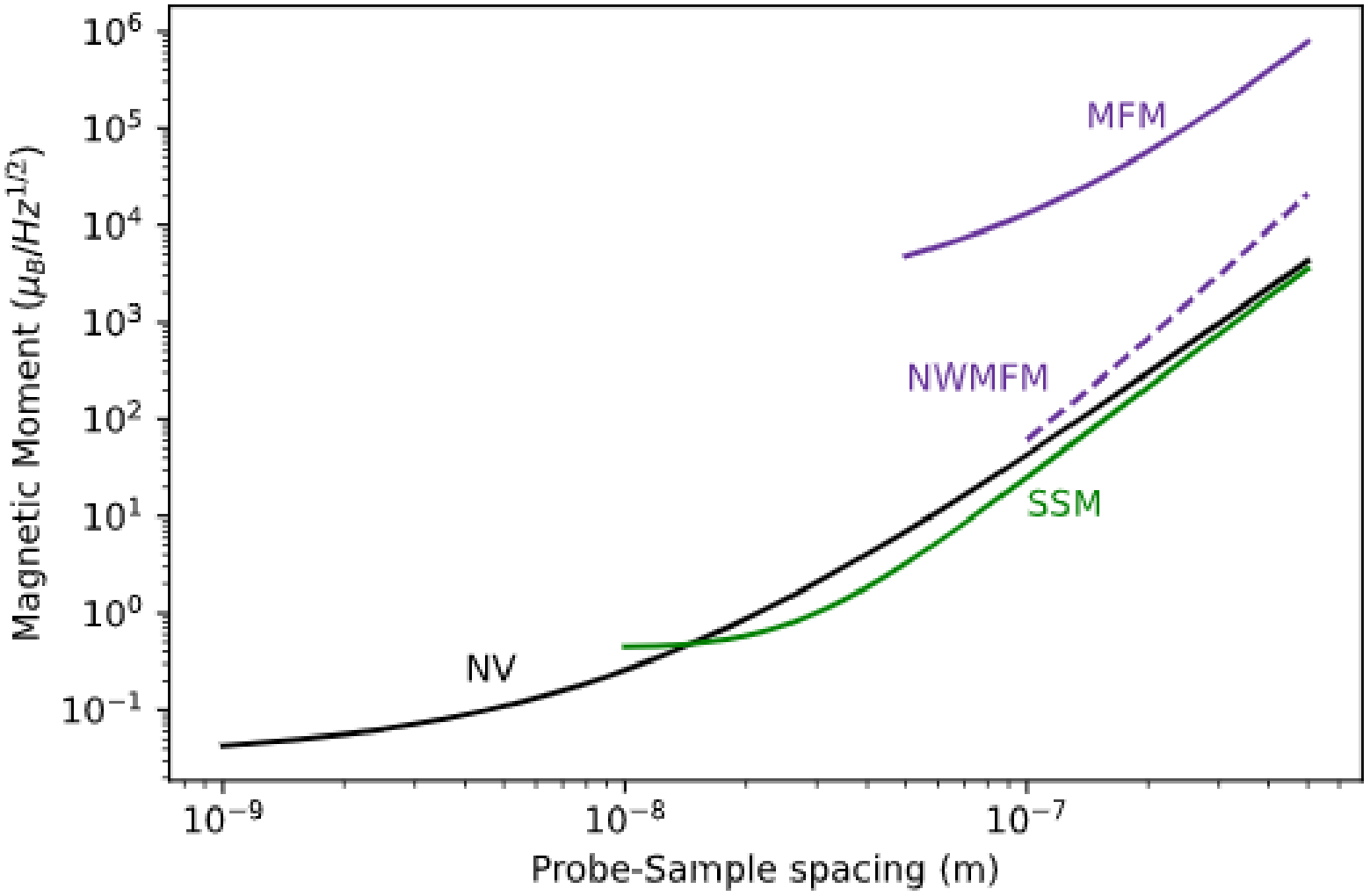

State of the Art

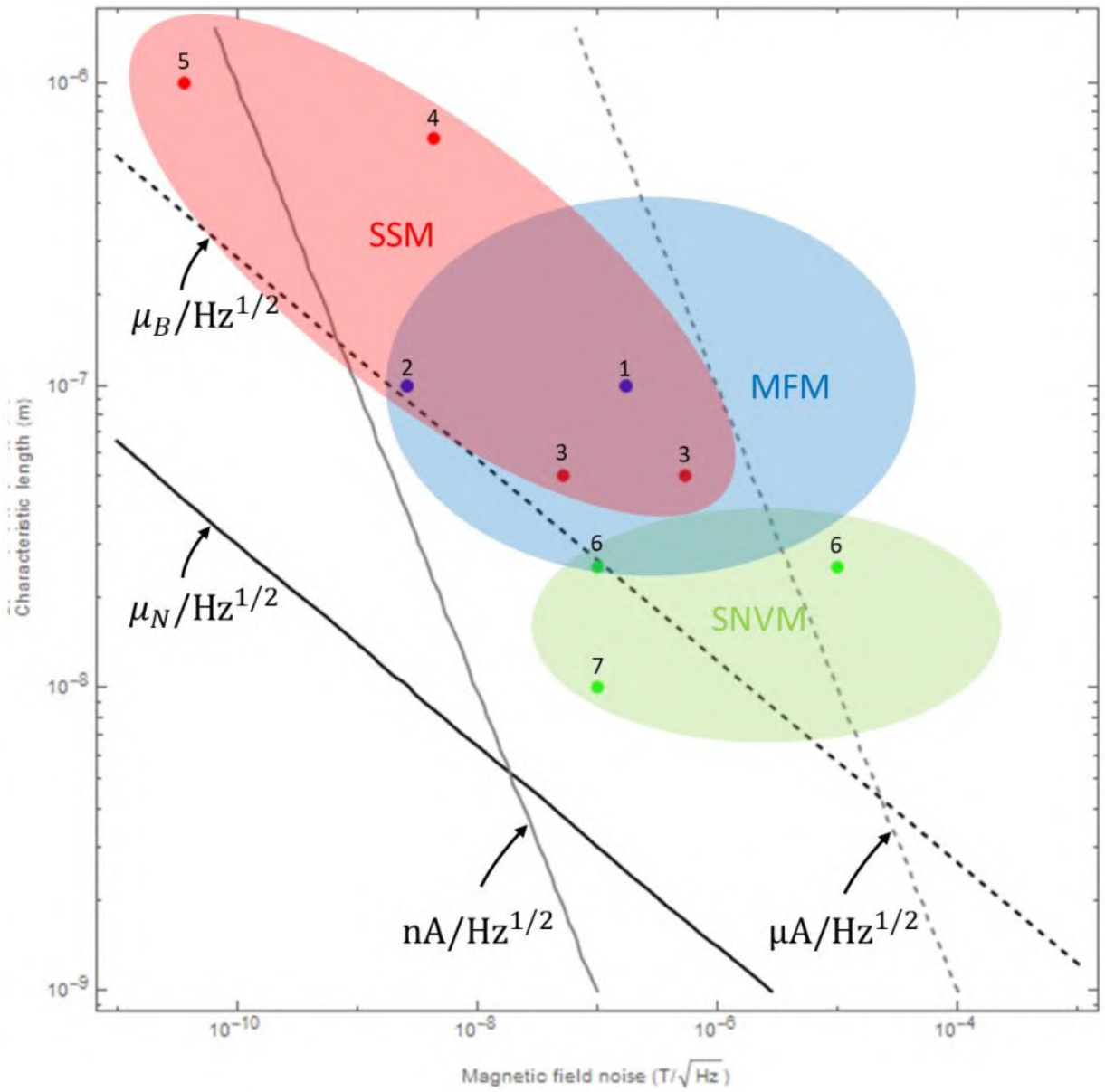

SQUID-on-lever (SOL)

Machining cantilevers by Focused Ion Beam (FIB)

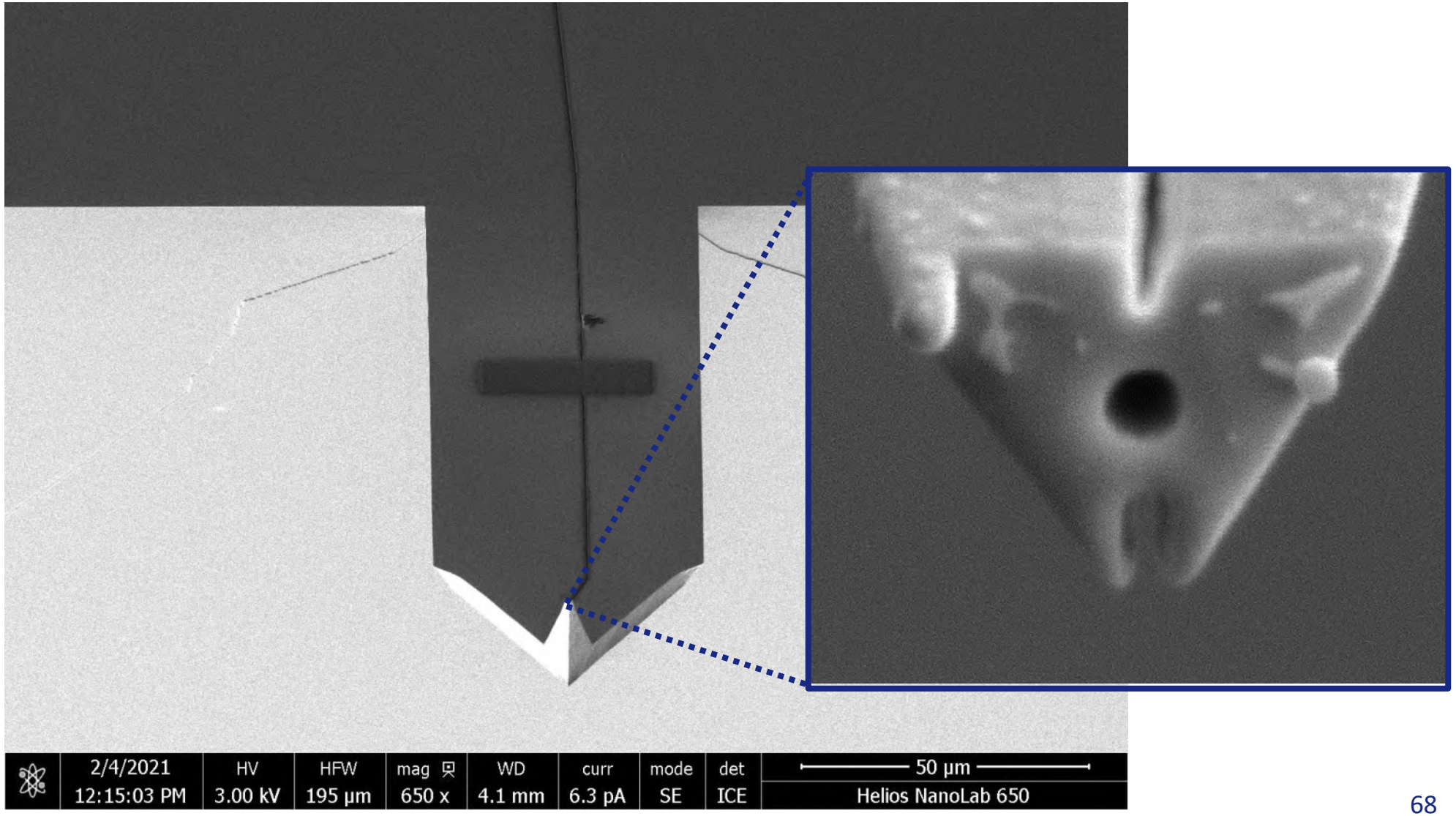

Focused Ion Beam fabrication of superconducting scanning Probes (FIBsuperProbes)

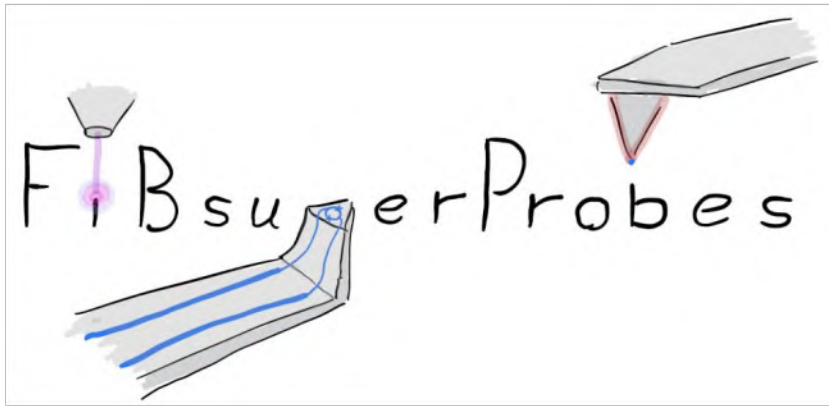

- 2020 - 2024
  - Basel (Coordinator)
  - CSIC Zaragoza
  - Tübingen
  - IBM Zürich

Universität Basel
CSIC
EBERHARD KARLS UNIVERSITÄT TÜBINGEN
IBM

POGGIO LAB

poggiolab.unibas.ch

University of Basel

Funding:

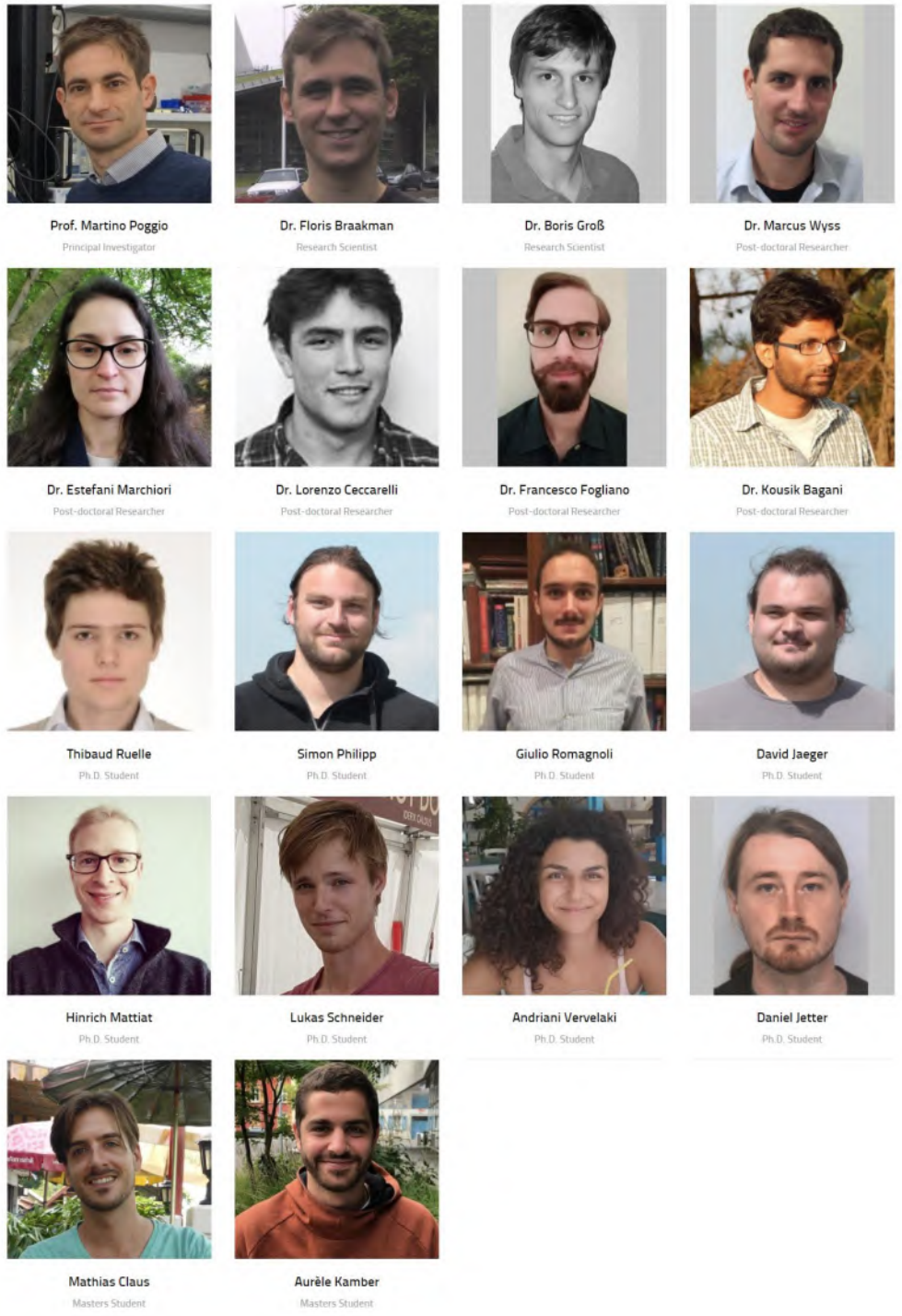

Zurich Instruments

Company profile

- Headquarters in Zurich, Switzerland
- Founded in 2008, 90+ people, 20+ nations
- Offices in China, USA, Italy, Korea, France
- Partners in Japan, Taiwan, Australia

→ Run by scientists for scientists

Zurich Instruments

Q&A

Thank you!

Prof. Martino Poggio
martino.poggio@unibas.ch

Dr. Jelena Trbovic
jelena.trbovic@zhinst.com

POGGIO LAB
poggiolab.unibas.ch

University of Basel

Zurich Instruments

PHYSICS TODAY

Zurich Instruments

Challenge us.

What are the requirements for your next project?

Contact us today

www.zhinst.com